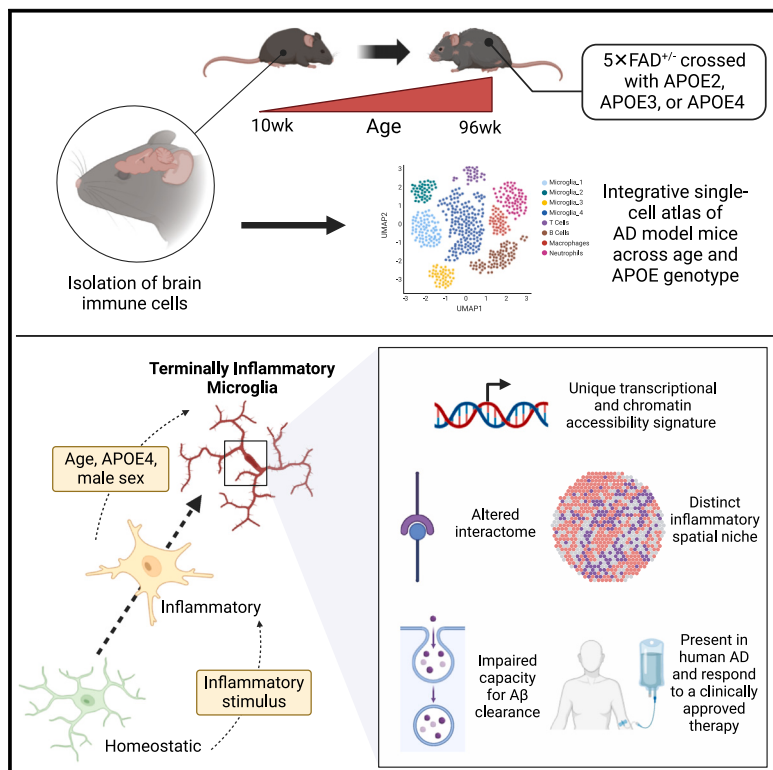


Immunity

An exhausted-like microglial population accumulates in aged and *APOE4* genotype Alzheimer's brains

Graphical abstract



Authors

Alon Millet, Jose Henrique Ledo,
Sohail F. Tavazoie

Correspondence

ledo@musc.edu (J.H.L.),
sohail.tavazoie@rockefeller.edu (S.F.T.)

In brief

Advanced age and the *APOE4* genetic variant are the dominant risk factors for late-onset Alzheimer's disease (AD). Millet et al. examine AD mouse models and identify a microglial population defined by expression of inflammatory signals and cell-intrinsic stress markers whose frequency increases with age and *APOE4* burden. This state, associated with functional defects, is found also in human AD.

Highlights

- Age and *APOE4* enrich for TIM, microglia co-expressing stress and inflammatory markers
- TIM are present in human AD and spatially colocalize with A β plaques in the cortex
- TIM are an exhausted-like population with impaired function and signaling
- Aducanumab treatment alters TIM heterogeneity and state in an *APOE*-dependent manner



Article

An exhausted-like microglial population accumulates in aged and *APOE4* genotype Alzheimer's brains

Alon Millet,^{1,2,4} Jose Henrique Ledo,^{1,3,4,*} and Sohail F. Tavazoie^{1,2,5,*}

¹Laboratory of Systems Cancer Biology, The Rockefeller University, New York, NY 10065, USA

²Tri-Institutional Program in Computational Biology and Medicine, The Rockefeller University, New York, NY 10065, USA

³Department of Pathology and Laboratory of Medicine, Department of Neuroscience, South Carolina Alzheimer's Disease Research Center, Medical University of South Carolina, Charleston, SC 29425, USA

⁴These authors contributed equally

⁵Lead contact

*Correspondence: ledo@musc.edu (J.H.L.), sohail.tavazoie@rockefeller.edu (S.F.T.)

<https://doi.org/10.1016/j.immuni.2023.12.001>

SUMMARY

The dominant risk factors for late-onset Alzheimer's disease (AD) are advanced age and the *APOE4* genetic variant. To examine how these factors alter neuroimmune function, we generated an integrative, longitudinal single-cell atlas of brain immune cells in AD model mice bearing the three common human *APOE* alleles. Transcriptomic and chromatin accessibility analyses identified a reactive microglial population defined by the concomitant expression of inflammatory signals and cell-intrinsic stress markers whose frequency increased with age and *APOE4* burden. An analogous population was detectable in the brains of human AD patients, including in the cortical tissue, using multiplexed spatial transcriptomics. This population, which we designate as terminally inflammatory microglia (TIM), exhibited defects in amyloid- β clearance and altered cell-cell communication during aducanumab treatment. TIM may represent an exhausted-like state for inflammatory microglia in the AD milieu that contributes to AD risk and pathology in *APOE4* carriers and the elderly, thus presenting a potential therapeutic target for AD.

INTRODUCTION

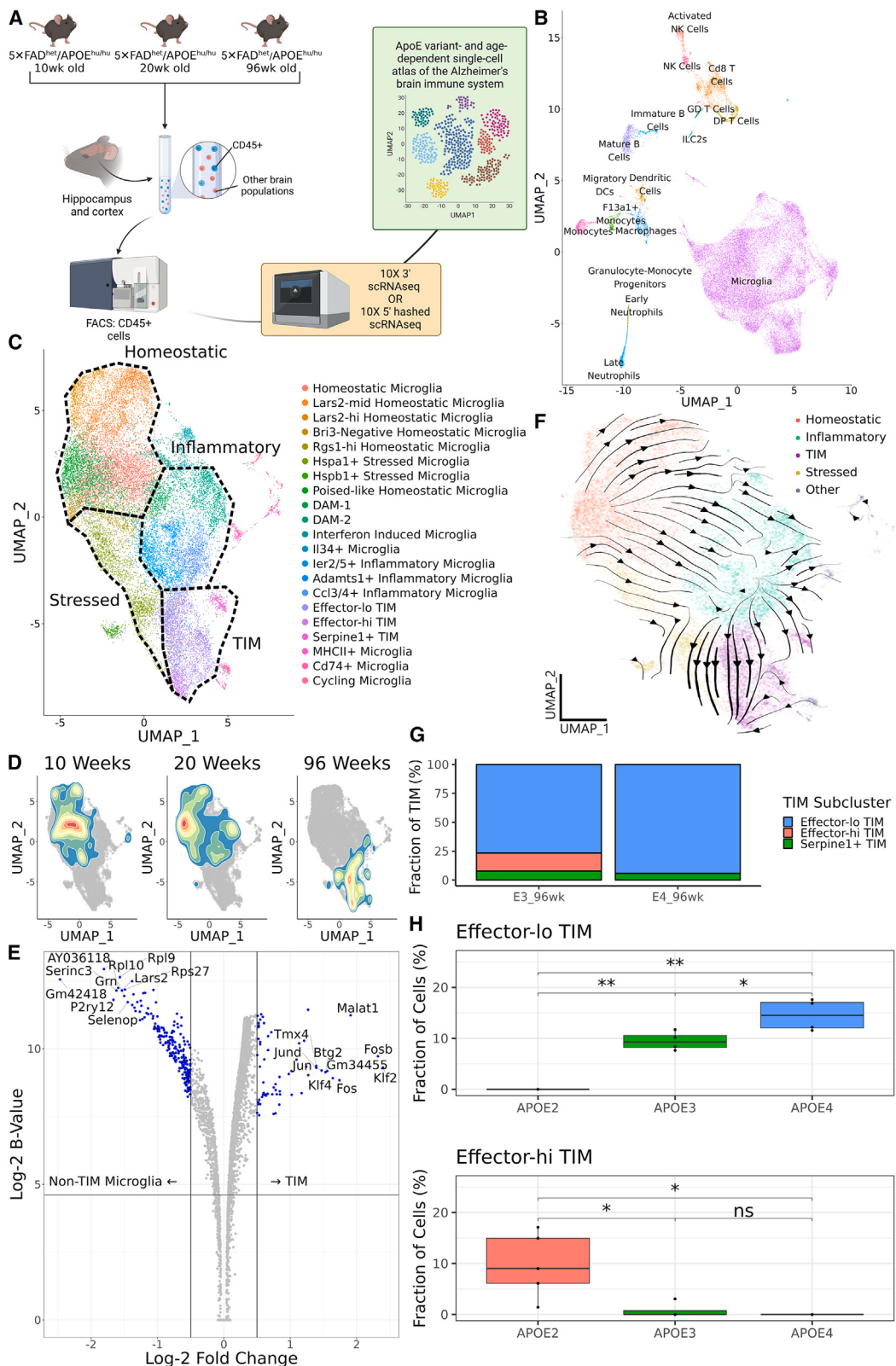
Alzheimer's disease (AD) is an incurable neurodegenerative disease and the predominant form of dementia, characterized by progressive synaptic dysfunction, neuronal loss, and cognitive decline.^{1,2} Excessive accumulation of the amyloid- β (A β) peptide and aggregates of hyperphosphorylated tau proteins are the major pathological features of the Alzheimer's brain, followed by neuroinflammation, which is thought to be driven primarily by microglial cells.^{1–3} Microglia are yolk-sac-derived myeloid cells and the dominant immune population of the brain.^{4–6} Although microglia are central mediators of classical neuroinflammation, they are also a highly heterogeneous population, existing in the AD brain in distinct states that can be differentially beneficial or detrimental to disease progression.^{7–14} Nonetheless, the factors determining whether a given microglial population either constrains or contributes to AD pathology remain poorly defined.

Apolipoprotein E (*APOE*) is a secreted protein named for its central role in lipid trafficking with three common human isoforms: *APOE2*, *APOE3*, and *APOE4*. Although these alleles only vary at two amino acid sites, they are nonetheless strongly associated with differential risk for several diseases, including hyperlipidemia and atherosclerosis.¹⁵ *APOE* is of particular inter-

est in human health due to its role as the single largest monoallelic risk factor for late-onset AD (LOAD), with *APOE4* increasing risk and *APOE2* reducing risk relative to *APOE3*, the most common allele in the population.¹⁶ *APOE* is also a regulator of immunity more broadly, with roles in anti-tumor immunity,^{17,18} the response to SARS-CoV-2 infection,¹⁹ and multiple other inflammatory contexts.²⁰ Still, the mechanisms by which brain immune cells are jointly modulated by aging and distinct *APOE* alleles are not well understood.

We aimed to characterize the immune cellular changes in the AD brain driven by aging and distinct *APOE* alleles by generating a single-cell atlas of immune cells from the brains of AD mice bearing *APOE2*, *APOE3*, or *APOE4* alleles at distinct ages. Our atlas encompasses mice from 10 weeks of age to ~2 years of age, an understudied super-elderly state. By combining two global genome-wide modalities across multiple time points in AD progression, we systematically profiled the complex dynamics of the neuroimmune system and leveraged these data to interrogate its emergent biological properties. We identified a population of microglia expressing a signature of inflammatory and stress signaling markers whose frequency was enriched by age and *APOE4* genotype. These microglia are present in human AD; exhibit impaired capacity for A β clearance; and appear to be



**Figure 1. The age- and APOE isoform-dependent AD neuroimmune atlas**

(A) Schematic of the workflow used to generate the atlas, generated from $n = 3\text{--}6$ animals per age and genotype.
 (B) UMAP of all cells in the atlas.

(legend continued on next page)

key participants in the microglial response to aducanumab, an approved AD treatment. These findings identify a putative exhausted-like state for microglia in AD and a potential target cell for future therapeutic intervention.

RESULTS

Single-cell RNA sequencing identifies a TIM state in AD mice

We crossed 5 \times FAD mice, a common murine model of AD progression, with mice bearing human APOE2, APOE3, or APOE4 alleles in the murine *Apoe* locus (hereafter denoted as AD * APOE2, AD * APOE3, and AD * APOE4). We flow-sorted Cd45 $^{+}$ cells from the hippocampal and cortical regions of these APOE-homozygote 5 \times FAD het mice at 10 and 20 weeks of age, as well as of APOE3- and APOE4-homozygote 5 \times FAD het mice aged to 96 weeks (~2 years, equivalent to a human octogenarian), pooling cells from 3 to 6 mice per group. We then performed 10X single-cell RNA sequencing (scRNA-seq) using either 3'v3 or 5'v2 capture technology, yielding an atlas of 30,868 single cells after filtering and quality control (Figure 1A). We sorted microglia specifically from hippocampal and cortical tissues due to their central roles in AD pathology and progression.^{3,21–23} Reciprocal principal component analysis mediated integration²⁴ followed by clustering identified 17 clusters, including one major cluster representing ~80% of single-cell profiles that expressed microglial markers⁸ such as *P2ry12* and *Tmem119* (Figures 1B and S1A). Subclustering this microglial group generated 20 discrete microglial subpopulations, including clusters corresponding to the disease-associated microglia (DAM) state²⁵ that were identified by high expression of genes such as APOE and *Cst7* (Figure 1C). We augmented these 20 clusters by leveraging a k-nearest neighbors (KNN) approach²⁶ to survey the single-cell manifold for small, highly connected groups of cells with unique expression signatures. After hierarchical statistical evaluation, a single high-confidence microcluster of 11 cells expressing a transcriptional program including interleukin (IL)-34 and *Ano1* passed thresholding (Figures S1B and S1C). We manually annotated this cluster as IL-34 $^{+}$ microglia, arriving at a final set of 21 clusters. To establish that the clusters identified in this pipeline are meaningful and not spurious products of overclustering, we trained a 100-ply random forest classifier on a 4-fold cross-validation scheme over 25 iterations on the raw count data from each cluster, using the classifier to produce a pairwise confusion matrix between each combination of microglial subclusters. Cells were rarely misassigned by this classifier (Figure S1D), supporting the final clustering generated by this approach.

We next asked whether some clusters were over- or under-represented in any samples. Although microglia appeared uniformly distributed by genotype in uniform manifold approximation and projection (UMAP) space after integration, microglia from 96-week-old mice showed a clear shift toward clusters marked by the concomitant expression of inflammatory genes such as *S100a8* and *S100a9* and immediate early response genes such as *Fos*, *Jun*, and *Egr1*²⁷ (Figures 1D, 1E, and S1E); we denote these clusters as terminally inflammatory microglia (TIM) (justification below). TIM were almost exclusive to samples from 96-week-old mice and particularly enriched in AD mice bearing the APOE4 genotype (45% of all microglia from AD * APOE3 at 96 weeks, 69% of all microglia from AD * APOE4 at 96 weeks, and <1% from all other samples; Figure S1F). Importantly, TIM were not a low-quality population or a group of doublets, as a spline-based miQC²⁸ approach scored cells from TIM clusters as less likely to be low quality ($p = 6.1 \times 10^{-33}$ by Mann-Whitney-Wilcoxon nonparametric test; Figure S1G) than cells from all other microglial clusters, even canonical populations such as DAM and homeostatic microglia.

Inflammatory microglia, the activated counterpart of homeostatic microglia, accumulate in the AD milieu due to persistent AD-associated neuroinflammation.^{14,29} Given the high frequency of TIM in aged samples and their near absence in younger mice, we reasoned that they may represent a more advanced stage for inflammatory microglia in the AD brain. To this end, we generated splice-aware alignments³⁰ and performed directed fate mapping using CellRank³¹ to construct a composite transition kernel. Splicing dynamics are powerful features for the study of cell transitions, as the ratio between spliced and unspliced products can inform whether genes are being stably expressed, being induced, or being repressed at the time of library preparation. However, we elected to design the kernel based heavily on connectivity and CytoTRACE³² with a comparatively minimal contribution from splicing dynamics, as the cell transitions being captured in our data occur on a much longer timescale than that of splicing regulation. Consistent with TIM representing a terminal state, CellRank identified a robust flow from homeostatic microglia through acutely and chronically inflammatory clusters and into the age-specific population (Figure 1F). Based on the above observations, we termed these cells TIM.

We noted that TIM partitioned into two major subpopulations, one that maintained a high expression of effector markers and one that instead exhibited a higher expression of stress markers; we termed these effector-hi TIM and effector-lo TIM, respectively (Figures 1C and S1A). The atlas suggested that effector-lo TIM might be enriched in AD * APOE4 and that effector-hi TIM might be enriched in AD * APOE3 (Figure 1G), but the statistical power to confirm this was lacking. We similarly questioned

(C) Subclustering and UMAP of microglia only.

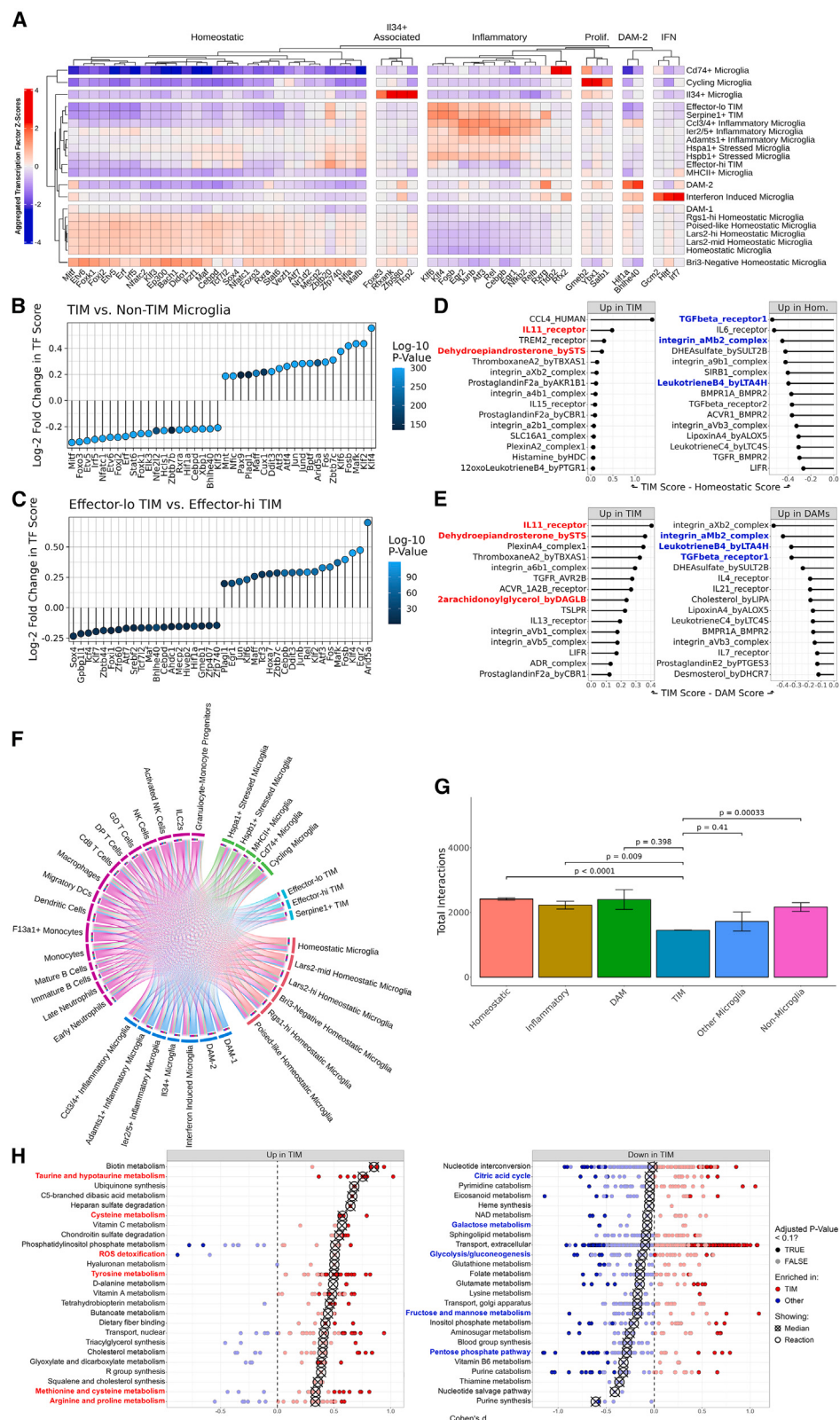
(D) 2D density plots overlaid on the microglial UMAP showing cell distributions at 10, 20, and 96 weeks of age.

(E) Volcano plot of differentially expressed genes between TIM and non-TIM microglia. The B-statistic is the log-odds that a gene is differentially expressed. Statistics were calculated using voom normalization and empirical Bayesian estimation through the limma package.

(F) CellRank-calculated velocity streams on data from 20- and 96-week-old mice. Streams were estimated by a custom kernel based on splicing dynamics, connectivity, and CytoTRACE. Cells are embedded on the same UMAP manifold as in (C).

(G) Stacked barplot of TIM subpopulations in the atlas from AD * APOE3 and AD * APOE4 animals at 96 weeks of age.

(H) Boxplots of the proportion of effector-lo and effector-hi TIM in bulk sequencing samples of 60-week-old AD * APOE animals, estimated by *in silico* decomposition with the atlas as a reference. Significance was evaluated by Welch's t test; * $p < 0.05$, ** $p < 0.01$.

**Figure 2. TIM are defined by a unique transcriptional program, interactome, and metabolic state**

(A) Heatmap of SCENIC-derived regulons per cluster, filtered to most highly variable transcription factors.

(B) Lollipop plot of differentially enriched SCENIC-derived regulons between TIM and all non-TIM microglia. Positive values indicate increased strength in TIM.

(legend continued on next page)

whether AD⁺APOE2, which was absent from the atlas at the 96-week time point, would display shifts in TIM subpopulations. To explore these questions, we aged a cohort of AD⁺APOE2, AD⁺APOE3, and AD⁺APOE4 mice ($n = 5$ per genotype) to 60 weeks and separately sorted Cd45⁺ cells from the hippocampal and cortical regions of each brain. We then generated bulk RNA-seq libraries from each of the 15 samples and used our single-cell atlas as a reference to perform *in silico* decomposition³³ of the bulk counts (Figures 1H and S1H). Consistent with our atlas, we found that AD⁺APOE4 mice were enriched for effector-lo TIM compared to their AD⁺APOE3 counterparts. Interestingly, although effector-hi TIM were not increased in AD⁺APOE3 compared with AD⁺APOE4, again consistent with our atlas, we found that essentially all TIM from AD⁺APOE2 mice were effector-hi in transcriptional signature. These findings demonstrate that TIM exhibit heterogeneity and that this heterogeneity is modulated in the context of AD by APOE genotype.

TIM are defined by distinct transcription factors, cell-cell contacts, and metabolic pathways

To better characterize the drivers of TIM and other microglial populations in our atlas, we used single-cell regulatory network inference and clustering (SCENIC)³⁴ to perform gene regulatory network reconstruction (Figure 2A). Hierarchical clustering of the most highly variable regulons recapitulated known features of microglial biology, such as the enrichment of an *Irf7*-driven regulon in a subcluster of microglia expressing interferon-associated genes³⁵ and *Hif1a* scoring highly in the late-stage DAM-2 cluster.³⁶ We found that a regulon defined by *Smad4*, which is required for microglial differentiation and development,³⁷ was significantly depleted in DAM relative to all other microglia in our atlas (Figure S2A), suggesting that DAM may acquire their phenotype through quasi-reversion to a border-associated macrophage-like state. Meanwhile, TIM were strongly associated both with a suite of inflammatory regulons driven by nuclear factor (NF)- κ B³⁸ and CEB/P³⁹ family transcription factors and with multiple AP-1 family transcription factors (Figures 2B and S2B). Interestingly, TIM were strongly enriched for some inflammatory regulons (*NfkB2*, *Irf1*, *Irf3*, and *Irf4*) but depleted for others (*Irf5*, *Irf7*, *Irf9*, and *Stat1/2*) relative to homeostatic microglia (Figure S2C), indicating potential selective regulation of specific inflammatory pathways. We additionally found that effector-lo TIM were distinguished from effector-hi TIM by the increased utilization of these AP-1 and Klf-family factors and comparatively weaker regulation through regulons such as *Sox4* and *Tcf4* (Figure 2C).

Although our brain immune atlas is dominated by microglia, it also includes several other immune populations that commingle with microglia in the AD milieu. We consequently aimed to model these contacts using cell-cell interaction imputation via CellPh-

neDB.⁴⁰ We compared ligand-receptor complexes with high predicted importance between TIM and both homeostatic (Figure 2D) and DAM (Figure 2E) clusters, nominating IL-11, dehydroepiandrosterone (DHEA), and 2-arachidonoylglycerol (2-AG) as strongly enriched and integrin α M β 2 (MAC-1) and leukotriene B4 as strongly depleted in TIM relative to both. IL-11, DHEA, and 2-AG have all been implicated as attenuators of microglial activation and mediators of remyelination and repair programs.^{41–43} Likewise, MAC-1 has been nominated as a key contributor to microglial activation and neurodegeneration in both AD⁴⁴ and other neurodegenerative conditions such as Parkinson's disease,⁴⁵ whereas leukotriene B4 is an established contributor to neutrophil infiltration and tissue damage.⁴⁶ Together, this shift in the interactome of TIM supports a bias toward decreased inflammation and reduced activation in comparison with other inflammatory populations such as DAM. Interestingly, transforming growth factor β (TGF- β) signaling was also predicted to be depleted in TIM compared with both DAM and homeostatic microglia despite TGF- β being a potent anti-inflammatory microglial cytokine,⁴⁷ suggesting an alternative mechanism by which TIM acquire a less inflammatory phenotype. In addition, consistent with the view that TIM skew less inflammatory in their cell state, we found that TIM were predicted to be significantly less promiscuous in their cell interaction networks than all other microglial populations (Figures 2F and 2G), indicating a diminished ability to contribute to inflammation in their local environment.

We next aimed to leverage scUTRQuant,⁴⁸ a pipeline that performs 3' UTR-sensitive alignment, to study differential 3' UTR length and intronic polyadenylation events in our data. Given our particular interest in TIM and their relative enrichment in AD⁺APOE4 mice over AD⁺APOE3 mice, we aligned and compared reads from AD⁺APOE3 and AD⁺APOE4 96-week-old mice. Several genes passed differential enrichment thresholding after bootstrapping, including immune-related genes (*Il13ra1* and *Apobec3a*), chromatin remodelers (*Rbbp4*), and a striking number of endocytosis-related and lysosomal genes (*Gimp*, *Rab7*, *Abcg1*, *Tubb5*, *Atp2b4*, and *Ppt1*) with significantly differentially regulated 3' UTR lengths and internal polyadenylation events between the two APOE genotypes (Figures S2D–S2F). Moreover, given the function of metabolism in supporting microglial states, we surmised that TIM would be defined by differential metabolic phenotypes when compared with other microglia. We therefore inferred the metabolic state of all microglia using Compass,⁴⁹ a flux balance analysis algorithm that estimates a model of bidirectional flow of all metabolic reactions in Recon2 weighted by the expression level of key metabolic enzymes (Figure 2H). Interestingly, pathways in cellular energetics such as the citric acid cycle; glycolysis/gluconeogenesis; the pentose phosphate pathway; and the metabolism of sugars such as galactose, fructose, and mannose were depleted in TIM, suggesting an

(C) Same as (B) but comparing effector-lo TIM with effector-hi TIM. Positive values indicate increased strength in effector-lo TIM.

(D) CellPhoneDB scores for ligand-receptor complexes, comparing TIM and homeostatic microglia.

(E) Same as (D) but comparing TIM and DAM.

(F) Circos plot of the atlas interactome. Size of the outermost bars represents the number of interactions, divided into cluster-by-other and other-by-cluster.

(G) Barplot showing the total number of interactions predicted to be made by each cluster. Superclusters follow the same division as in (F). Bars are means \pm standard error, and significance was evaluated by Welch's t test.

(H) Dot plot of the Cohen's d of Compass scores for metabolic pathways, comparing TIM with non-TIM microglia. Each point represents a reaction within the larger subsystem; subsystems are sorted by median enrichment value. Medians are indicated by crossed points.

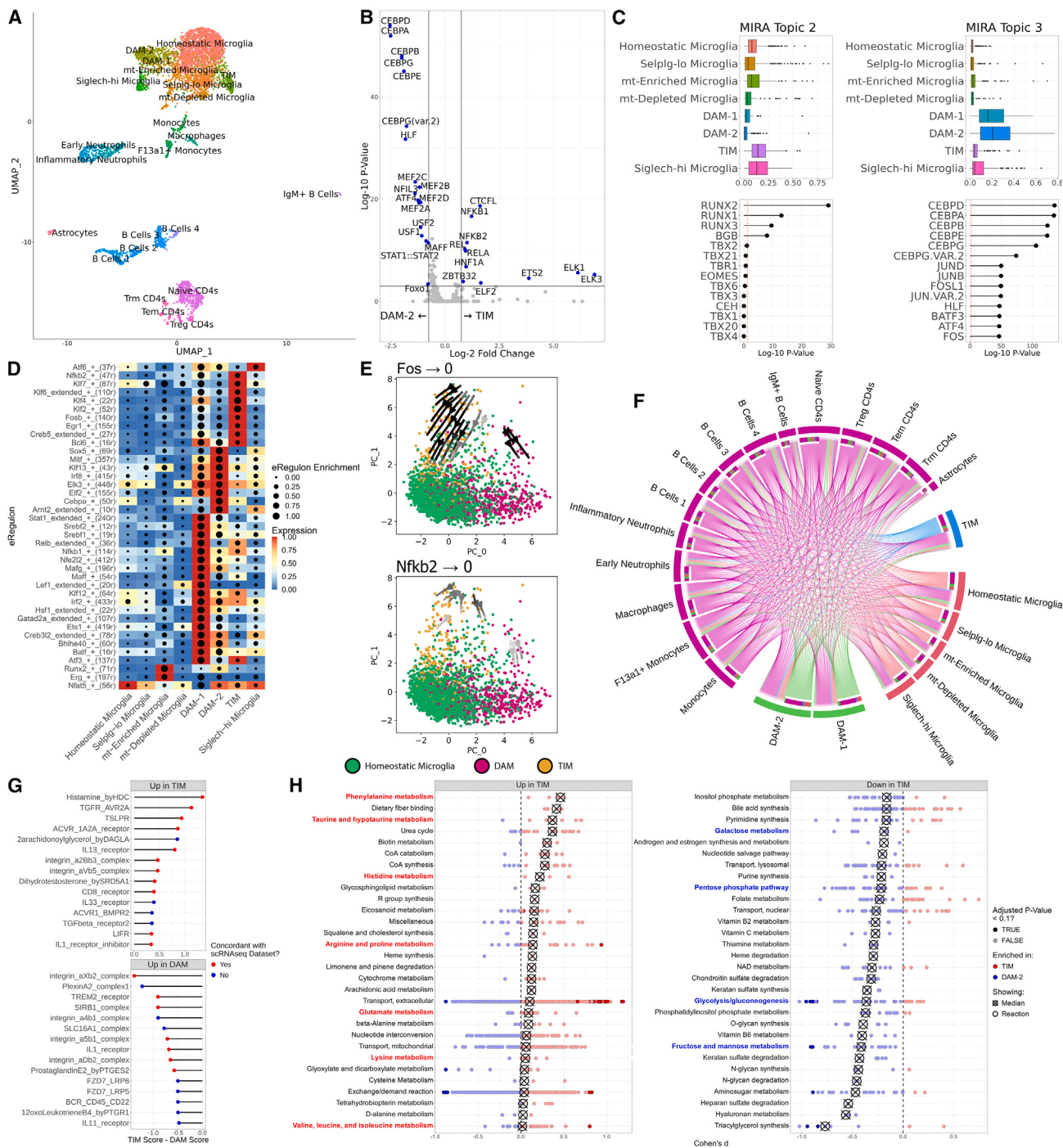


Figure 3. Multiome sequencing of *AD⁺APOE4* mice at 60 weeks of age nominates regulatory features of TIM

(A) Joint UMAP of RNA and ATAC features from the multiome library.

(B) Volcano plot of chromVAR motif accessibility between TIM and DAM-2 cells.

(C) Scores for two topics derived from the latent Dirichlet allocation of ATAC features and their associated transcription factors.

(D) Heatmap of eRegulon enrichment and expression across microglial clusters.

(E) Perturbation simulation plots ablating *Fos* and *Nkfb2*. Expression of the respective transcription factor was set to 0, and the gene regulatory networks were re-initialized to generate new expression profiles for each cell. Cells are projected in a PCA space defined by the gene regulatory net. Arrow shade indicates the magnitude of the transition flow.

(F) Circos plot of the multiome dataset interactome. Size of the outermost bars represents the number of interactions, divided into cluster-by-other and other-by-cluster.

(legend continued on next page)

energetic deficiency unique to this population. Meanwhile, TIM were enriched for pathways in detoxification of reactive oxygen species and in the metabolism of several amino acids, including taurine, hypotaurine, cysteine, tyrosine, methionine, arginine, and proline, implicating altered glutathione and amino acid metabolism as key features of the TIM state.

Single-cell multiome sequencing uncovers mediators of transcriptional regulation in TIM

Collectively, these data suggested that TIM are a distinct population of microglia that arises exclusively in aged mice and with higher frequency in AD⁺APOE4 than in AD⁺APOE3. However, our atlas lacked resolution in the period between 20 and 96 weeks, when TIM transition from being essentially absent to being nearly dominant, limiting our ability to predict the determinants of TIM emergence. Moreover, the atlas was restricted only to transcriptomic space, reducing the confidence with which claims about gene regulation could be made, and was generated by integrating both 3' and 5' libraries, an approach that makes assumptions about capture efficiency and library preparation. We therefore complemented the atlas by using 10X snRNA-seq/scATAC-seq multiome sequencing to jointly characterize the transcriptome and the chromatin accessibility landscape of Cd45⁺ cells sorted from the hippocampal and cortical regions of AD⁺APOE4 mice aged to 60 weeks. We elected to perform multiome sequencing on samples from AD⁺APOE4 mice to maximize the likelihood of detecting TIM at this intermediate time point. After filtering and quality control,⁵⁰ the resulting library consisted of 5,081 single-cell profiles across 32,285 RNA species and 134,523 differentially accessible regions. Joint representation of RNA and ATAC features followed by clustering identified 23 clusters, 8 of which were microglial subclusters (Figure 3A). Confirming our results from the age- and APOE isoform-dependent atlas, one cluster in these 60-week-old mice was defined by a gene expression program corresponding to that of TIM and was present at a frequency of 7.3% of all microglia, more frequently than in 20-week-old mice (0.3%) and less frequently than was detected in 96-week-old mice (69%) (Figures S3A and S3B). These findings indicate that TIM are already present at robustly detectable levels by 60 weeks of age and continue to accumulate thereafter in an age-dependent manner. Reassuringly, both RNA and ATAC modalities had high concordance in markers for TIM, such as *Egr1* and *Btg2* (Figure S3C), and in well-established markers in other clusters such as APOE for DAM, *Skap1* for T cells, *Ngp* for neutrophils, and *Ebf1* for B cells (Figure S3D). Further validating results from the atlas, transcription factor footprinting of *CEBPD*, a predicted regulon in DAM, and *NFKB2*, a predicted regulon in TIM, showed higher Tn5 insertion enrichment in their respective clusters (Figures 2A and S3E).

To leverage chromatin accessibility information from the multiome dataset, we used chromVAR⁵¹ to unbiasedly profile the chromatin landscape and infer motif accessibilities in each cell.

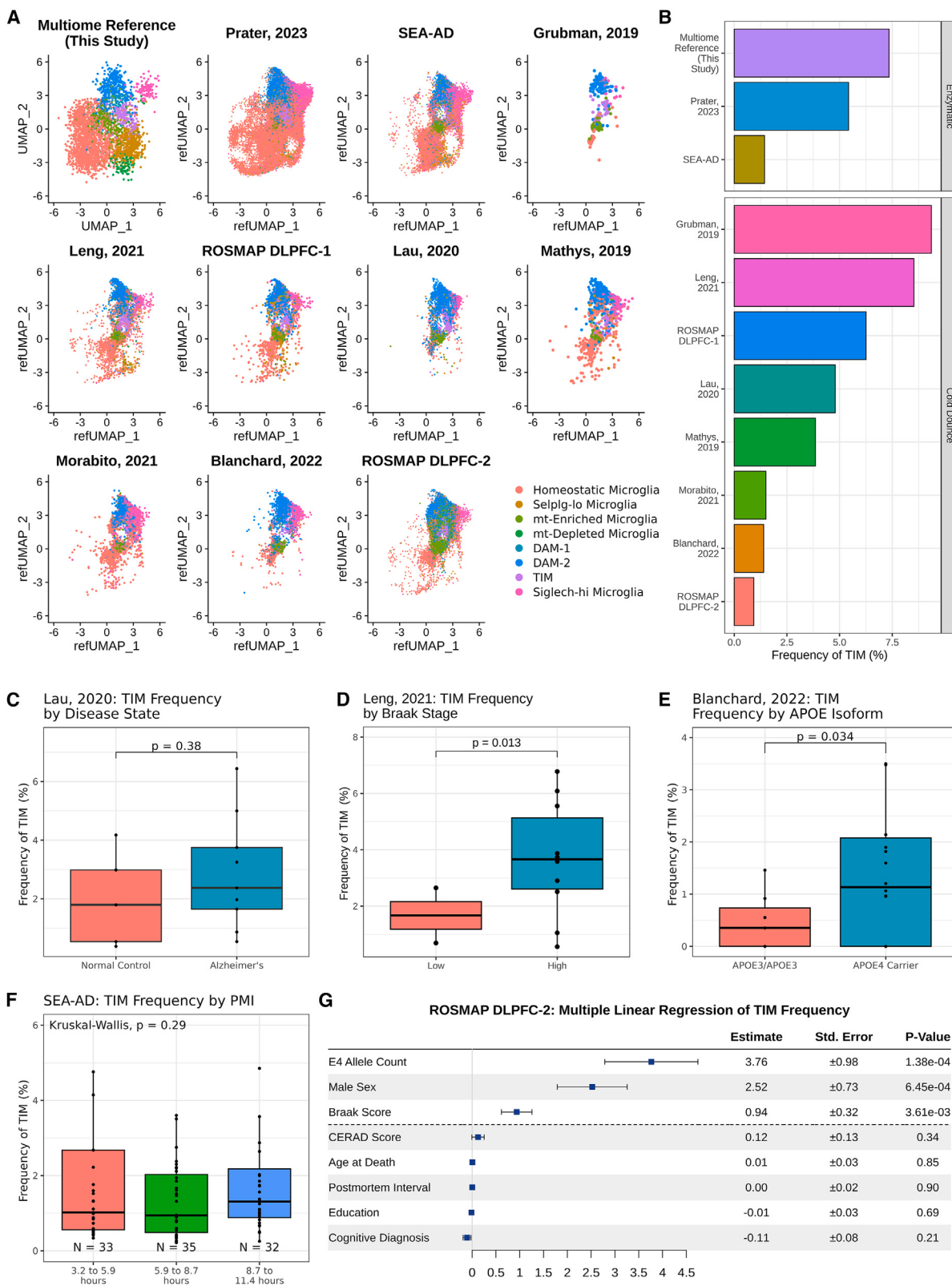
In addition to the motifs we previously identified by footprinting, ETS family motifs were nominated as uniquely enriched in TIM compared with other clusters (Figure 3B). As a more sophisticated alternative to naive enrichment, we also performed latent Dirichlet allocation-based topic modeling⁵² of RNA and ATAC features, identifying 11 RNA topics and 20 ATAC topics that captured the dynamics of multiomic regulation across the entire dataset (Figure 3C). Of these, ATAC topic 2 (defined by RUNX factors) was enriched in TIM, whereas ATAC topic 3 (defined by both CEB/P factors and AP-1 factors) was enriched in DAM.

We then aimed to capture the gene regulatory networks undergirding the accumulation of TIM by using the SCENIC+ suite⁵³ to model transcription factor “enhancer regulons,” or eRegulons, contributing to cell state in each cluster (Figure 3D). Consistent with the above-mentioned results, TIM scored highly for *NfkB2* and *Fos* eRegulons, whereas DAM scored highly for *Cebpa* and *Sox5* eRegulons. We reasoned that these regulatory networks were strong drivers of their respective cell clusters and that their ablation would be sufficient to drive these two cell populations back to a homeostatic state. To test this, we performed computational perturbation simulations of the SCENIC+ gene regulatory network by artificially setting the expression of the given transcription factor to 0, recalculating the expression of all other genes based on the SCENIC+ gene regulatory network, and embedding the resulting cells on a PCA manifold constructed from eRegulon information. The ablation of *Fos* and *NfkB2* signaling produced a robust flow from TIM back onto the homeostatic cluster (Figure 3E), whereas the ablation of *Sox5* likewise generated a flow from DAM back onto the homeostatic cluster (Figure S3F). Interestingly, the ablation of other regulons associated with the TIM state such as *Klf4* did not produce concordant shifts in gene regulatory network status (Figure S3G), suggesting that *Fos* and *NfkB2* may be required for TIM maintenance, whereas *Klf4* and other factors might be dispensable once the TIM state is attained.

Seeking to replicate the results from the integrated atlas, we modeled cell-cell interactions in the multiome dataset with CellPhoneDB. In agreement with the findings from the atlas, we identified fewer interactions made by TIM than by either homeostatic microglia or DAM (Figure 3F). Moreover, many of the differentially enriched complexes from the atlas, such as DHEA, TGF-β, and 2-AG, were among the strongest contributors to the microglial interactome in the multiome dataset (Figure S3H). A direct comparison of TIM to DAM in the multiome dataset identified a number of ligand-receptor pairs that were differentially enriched in each, the bulk of which were concordant in directionality with results from the larger dataset (Figure 3G). The most strongly enriched ligand in TIM in the multiome dataset, histamine, was concordant with the atlas and is implicated in microglial inflammation,^{54,55} consistent with the view of TIM as an inflammatory state. Meanwhile, DAM were strongly enriched for TREM2, a known driver of DAM progression⁹ and again concordant with the atlas. We similarly aimed to model

(G) CellPhoneDB scores for ligand-receptor complexes, comparing TIM and DAM. Points are colored based on whether the complex was also found to be differentially enriched in the atlas.

(H) Dot plot of the Cohen's d of Compass scores for metabolic pathways, comparing TIM with DAM-2s. Each point represents a reaction within the larger subsystem; subsystems are sorted by median enrichment value. Medians are indicated by crossed points.

**Figure 4.** TIM are detected in publicly available human snRNA-seq datasets

(A) UMAP projection of microglia from ten publicly available human snRNA-seq datasets after anchor integration onto the data acquired in this study.

(legend continued on next page)

the metabolic state of microglia in the multiome dataset using Compass to explore pathways with differential flux between TIM and DAM. Corroborating results from the atlas, TIM were markedly enriched for metabolic pathways of multiple amino acids, including taurine, hypotaurine, phenylalanine, histidine, arginine, proline, glutamate, lysine, cystine, alanine, valine, leucine, and isoleucine, whereas energetic pathways such as glycolysis; pentose phosphate pathway; and the metabolism of fructose, mannose, and galactose were strongly depleted in TIM compared with in DAM (Figure 3H).

TIM are pervasive in late-stage human AD and enriched by age and APOE4

Previous efforts utilizing murine models to describe microglial subpopulations in AD have frequently been constrained by the absence of equivalent populations in human samples; for instance, DAM are observed across murine AD models but have no single analog in human AD.⁵⁶ We consequently asked whether the TIM phenotype was unique to our aged mouse model or whether it might also be detectable in single-cell data gathered from human patients. To address this question, we used Seurat anchor integration for label transfer to project microglia from ten previously published snRNA-seq human brain datasets^{57–66} onto our murine multiome data (Figure 4A). TIM were identified in all ten datasets at frequencies comparable to that of the multiome reference; moreover, TIM were identified regardless of whether the tissue was processed by enzymatic digestion or by cold Dounce homogenization, indicating that the TIM state is not exclusively a product of *ex vivo* stress during sample preparation (Figure 4B). We next leveraged these integrations to query the accompanying metadata and explore the impact of various factors on the frequency of TIM. Consistent with our expectations, TIM were more abundant in samples from patients with AD than in samples from individuals without disease (Figure 4C); in samples from patients with more advanced disease as measured by Braak stage, a histopathological proxy for AD progression (Figure 4D); and in samples from patients carrying an APOE4 allele compared with their APOE3/APOE3 counterparts (Figure 4E). Importantly, the frequency of TIM did not correlate with post-mortem interval (Figure 4F), suggesting that TIM are unlikely to be an artifact of sample preparation. To better model the interplay of all these factors, we built a multiple linear regression model of TIM frequency across all individuals in the second ROSMAP dorsolateral prefrontal cortex project, a repository of snRNA-seq data from the dorsolateral prefrontal cortex of 465 human AD donors; again, consistent with our observations, we found that the APOE4 allele count and Braak score were strong predictors of TIM frequency, whereas other factors such as post-mortem interval had no predictive power (Figure 4G). Strikingly, we also observed that male sex was nearly

as strong a modifier of TIM frequency as APOE4 allele count in this dataset, suggesting the existence of a sex-specific phenotype controlling the emergence of this unique cell state. We note that although age at death was not a robust predictor of TIM frequency, >91% of samples in the dataset are from individuals over the age of 80, making it a poorly informative parameter in this analysis. Finally, we performed label transfer between our larger single-cell atlas and microglia from the Tabula Muris Se-nis, a single-cell atlas of mouse tissues across age.⁶⁷ We found that the frequency of TIM increased monotonically from 3-month-old to 24-month-old mice, in agreement with the view that TIM accumulate with age (Figure S4). These findings suggest that TIM are also present at robustly detectable levels in human brains and that their frequency follows the same trends as in mice with respect to age, disease, and the presence of the APOE4 allele.

The TIM spatial niche is enriched for A β plaques and inflammatory cells in the cortex

To further examine TIM in the context of human AD, we used the Xenium platform to perform multiplexed *in situ* transcriptomics on cortical tissue samples from six human AD donors, three homozygous for APOE4 and three homozygous for APOE3. After quality control and filtering,⁶⁸ the resulting dataset covered 494,376 individual cells over a panel of 266 genes. We leveraged our computational label transfer of previously published human snRNA-seq datasets to identify putative markers of human TIM during the annotation process (Figure S5A), yielding 22 clusters covering both neuronal and glial populations (Figures S5B and S5C). Critically, we observed a clear population of TIM with robust representation across both genotypes (Figures 5A). Consistent with our murine data, we found that donors homozygous for APOE4 were enriched for TIM relative to those homozygous for APOE3 (22.7% vs. 5.2%; Figure 5B). We generated a cell-cell spatial neighborhood matrix across all six sections, confirming that our data had captured the expected architecture of the cortex (Figure S5D). We then investigated the spatial niche of TIM within the tissue by calculating the increased probability of observing a given cell type near a TIM compared with the null distribution. We found that TIM are about 50% more likely to be found next to other TIM than would be expected based on their frequency, whereas L5 neurons and two astrocyte populations with a high copy number of APP or APOE transcripts were 10%–20% more likely than expected to be found next to TIM (Figures 5C and S5E). We repeated the same analysis in a genotype-aware fashion, revealing that TIM in APOE4 donors were more likely to cluster with neurons and these two astrocyte populations, whereas TIM in APOE3 donors were more often adjacent to oligodendrocytes, the majority of which reside in the white matter (Figure 5D). These data suggest that the

(C) Boxplot of TIM frequency in data projected from Lau et al.,⁶⁰ grouped by disease state. Significance was evaluated by Welch's t test.

(D) Boxplot of TIM frequency in data projected from Leng et al.,⁶¹ grouped by Braak stage, a measure of disease severity. Significance was evaluated by Welch's t test.

(E) Boxplot of TIM frequency in data projected from Blanchard et al.,⁵⁷ grouped by either amyloid- β burden or by the presence of an APOE4 allele. Significance was evaluated by Welch's t test.

(F) Boxplot of TIM frequency in data projected from the Seattle AD Brain Atlas, grouped by post-mortem interval. Significance was evaluated by Kruskal-Wallis test.

(G) Multiple linear regression of TIM frequency by metadata provided in the second ROSMAP dorsolateral prefrontal cortex (n = 465).

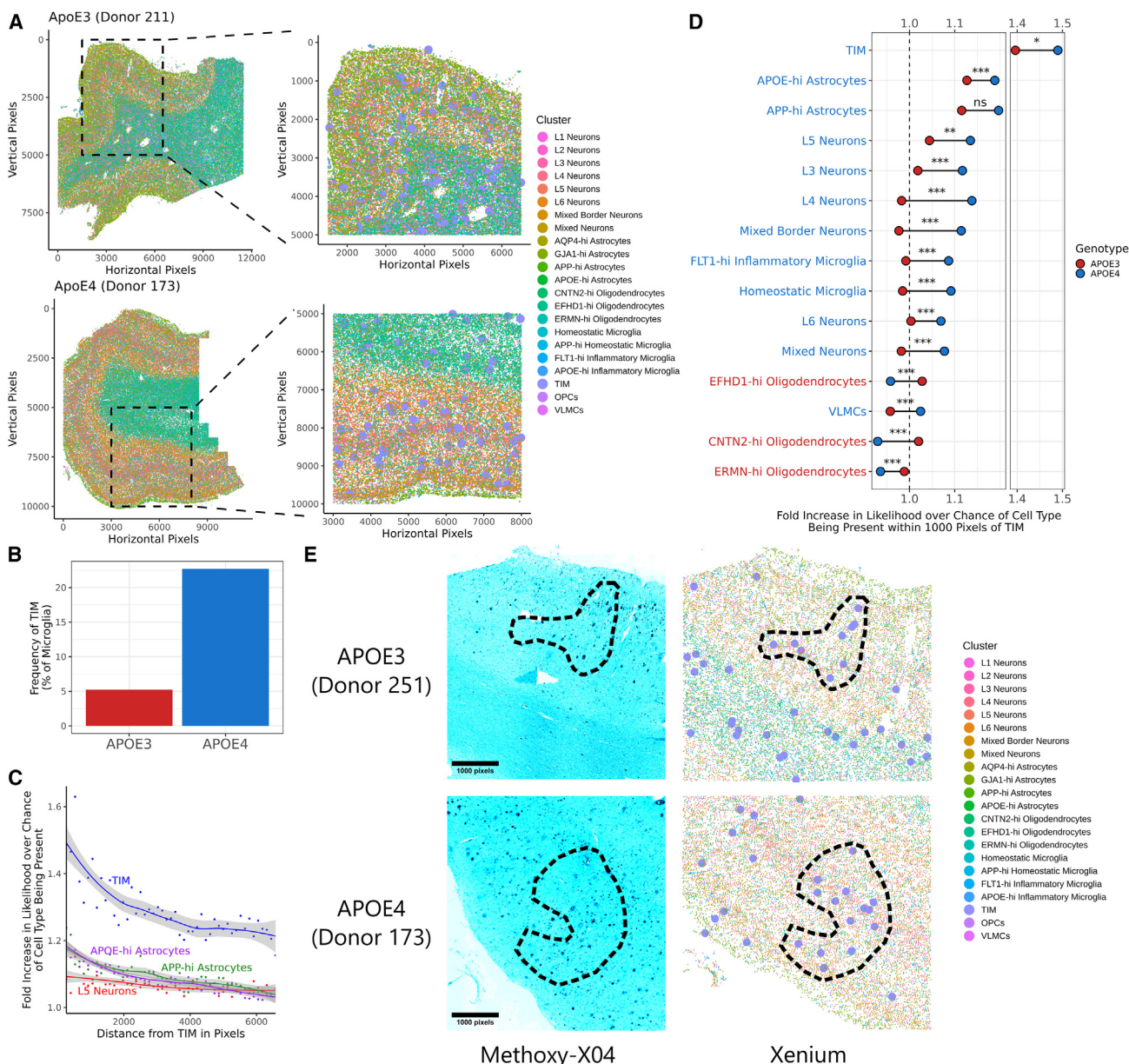


Figure 5. TIM are enriched in the cortical layers of human AD patients bearing ApoE4

(A) Spatial scatter plot of cell annotations in two representative sections out of the six subjected to Xenium analysis. At left is the full section, and at right is a zoomed inset of the indicated region. TIM are marked by larger point sizes in the zoomed inset for clarity.

(B) Barplot of the fraction of microglia from each genotype annotated as a TIM.

(C) Smoothed trendlines of the increased likelihood of finding a given cell type within a circle of the indicated radius centered on a TIM compared with over base expectation. Only the top four most enriched clusters are shown.

(D) Barbell plot showing the increased likelihood of finding a given cell type within a circle of the indicated radius centered on a TIM compared with base expectation, separated by genotype. Significance was evaluated by Welch's t test; * $p < 0.05$, ** $p < 0.01$, *** $p < 0.001$. Clusters are colored based on which genotype shows higher enrichment around TIM.

(E) Representative fluorescence micrographs of cortical tissue sections from APOE3 and APOE4 donors after post-Xenium staining with methoxy-X04 (a stain for A β) and accompanying annotations from Xenium data. TIM are marked by larger point sizes in the Xenium annotations for clarity. Circled regions indicate areas of high overlap between TIM and A β plaques.

APOE4 genotype is associated with both an increased frequency of TIM and an increased proximity of those TIM to gray matter. We then stained the same tissue sections used for Xenium with methoxy-X04, a fluorescent stain specific for A β pla-

ques. Comparing results from methoxy-X04 staining to our Xenium annotations revealed that TIM could be detected in regions containing high A β burden (Figure 5E), suggesting a potential role for TIM in A β -related pathogenesis.

TIM exhibit a defective capacity for A β phagocytosis and clearance

Collectively, our findings suggested that the TIM state might have consequences on microglial function and phenotype. To test this prediction, we harvested cells from the hippocampal and cortical regions of AD**APOE2*, AD**APOE3*, and AD**APOE4* mice at 60 weeks of age and incubated them *ex vivo* with fluorescently labeled and oligomerized A β 1–42. We employed a pH-insensitive fluorophore, HiLexa 488, to ensure that fluorescent signal would be stable after cellular uptake. We then sorted Cd45 $^{+}$ cells, splitting each sample into two tubes based on A β uptake as measured by fluorescent signal, before performing post-sort cell hashing followed by 10 \times 5'v2 scRNA-seq (Figure 6A). Filtering, quality control, and computational integration resulted in a dataset of 12,613 cells, 76% of which fell into one of 12 microglial subclusters and 24% of which fell into one of 17 smaller non-microglial populations (Figure 6B). Comparing the relative distribution of microglia from A β -hi and A β -lo pools revealed that the A β -lo population was qualitatively shifted away from homeostatic clusters and toward TIM (Figure 6C). We then examined the relative proportion of cells in each cluster that originated in the A β -hi pool per genotype to identify which populations were the most or least capable of A β uptake (Figure 6D). Two populations, one of homeostatic microglia enriched for ribosomal transcripts ($\chi^2_{0.05} = 1.88 \times 10^{-58}$) and one of microglia marked by interferon responsive genes ($\chi^2_{0.05} = 2.70 \times 10^{-17}$), were consistently overrepresented in the A β -hi pool, although interferon-induced microglia from AD**APOE4* were less overrepresented than their AD**APOE2* and AD**APOE3* counterparts. Meanwhile, both effector-lo TIM ($\chi^2_{0.05} = 6.87 \times 10^{-27}$) and effector-hi TIM ($\chi^2_{0.05} = 1.58 \times 10^{-14}$) were underrepresented in the A β -hi pool. Strikingly, AD**APOE4* was defined by both a more severe underrepresentation of effector-lo TIM in the A β -hi pool—suggestive of a more exacerbated defect in A β clearance by this population in this genotype—and a higher frequency of effector-lo TIM overall, revealing a compounding effect in which AD**APOE4* is overburdened with a population of particularly impaired cells.

The frequency and interactome of TIM are modulated by aducanumab treatment

Although AD remains incurable, aducanumab is a recently developed and approved monoclonal antibody therapeutic that aims to slow disease progression by selectively binding to A β aggregates.⁶⁹ It is believed that these aggregates are then cleared by Fc-receptor-mediated binding with myeloid cells. Although clinical trials showed modest improvements in cognition driven by treatment, patients nonetheless experienced significant side effects such as neuroinflammation and edema.⁷⁰ Given aducanumab's strong impact on myeloid cells in the AD brain, we wondered how it would influence the emergence and behavior of TIM in late-stage disease. We treated 60-week-old AD**APOE2*, AD**APOE3*, and AD**APOE4* mice with daily intraperitoneal injections of aducanumab or of an isotype control for 5 days before performing single-cell sequencing of Cd45 $^{+}$ cells from their hippocampal and cortical regions (Figure 7A). Processing and annotation produced a dataset of 13,483 cells, 80% of which were microglia (Figure 7B). Subclustering to microglia revealed that cells from animals treated with isotype control were predom-

inantly homeostatic, acutely inflammatory, or effector-lo TIM, whereas those from animals treated with aducanumab were instead largely DAM, effector-hi TIM, and poised-like homeostatic microglia (Figures 7C and 7D). Poised-like homeostatic microglia are differentiated from homeostatic microglia by a higher expression of major histocompatibility complex class I (MHC class I) genes and *Cd52* (Figure S6A), a gene signature associated with the microglial response to demyelination or injury.⁴

We used CellChat⁷¹ to better understand the shifts in the interactome driven by both aducanumab and *APOE* isoform across these samples, finding that aducanumab treatment and *APOE4* were both associated with a higher number of predicted interactions and a stronger average predicted interaction strength (Figure 7D). Querying across specific pathways identified key pathways with both high activity and differential utilization across *APOE* isoform (Figure 7E); for instance, *Gas6*, a major driver of inflammation implicated in A β plaque clearance,⁷² was more active after aducanumab treatment in *APOE3* and *APOE4*, whereas *Cd22*, a potent inhibitor of microglial phagocytosis,⁷³ was more active in *APOE2* after treatment. These findings suggest that aducanumab treatment was less able to drive microglial responses to A β in *APOE2* animals than in *APOE3* or *APOE4* counterparts. We then projected all ligand-receptor complexes onto a unified functional similarity manifold and determined the pairwise Euclidean distance between pathways from aducanumab-treated and isotype-control-treated animals of the same genotype (Figure 7F), revealing that *APOE2* mice exhibited the strongest shifts in signaling in *Cd22*, whereas *APOE3* and *APOE4* instead had shifts in *Cd39*, a regulator of microglial migration,⁷⁴ and *Csf1r*, a key microglial survival factor.⁷⁵

Next, we examined interactome shifts within specific cell types driven by aducanumab treatment. Strikingly, aducanumab massively expanded the total interactome of adaptive immune cells across all three genotypes, particularly Cd8 T cells and immature B cells (Figure S6B), both of which inhabit the dura of the meninges.^{76–78} Moreover, the interactome of these cell types was expanded in *APOE4* animals to a greater extent than in *APOE2* or *APOE3* animals. A closer examination of the Cd8 T cell interactome revealed that this was driven primarily by increases in inflammatory signaling through type-II interferons along with elevated cell-cell adhesion via ICAMs (Figure 7G). Similar pathways were also modulated in immature B cells, effector-lo TIM, and effector-hi TIM (Figure S6C). Finally, we explored which cell types might be driving differential T and B cell signaling after aducanumab treatment by separating signaling into senders and receivers and finding the mean difference in signaling strength between aducanumab-treated and isotype-control-treated animals across all *APOE* isoforms (Figure 7H). As expected, inflammatory microglial clusters showed the strongest increase in signal sending after aducanumab treatment. Remarkably, however, the largest growth in signaling after aducanumab treatment came from effector-hi TIM, suggesting that this population may be particularly critical while coordinating cell-cell communication networks during inflammation. Combined with the higher frequency of effector-hi TIM in aducanumab-treated animals, these findings highlight effector-hi TIM as central orchestrators of the adaptive immune response to aducanumab therapy.

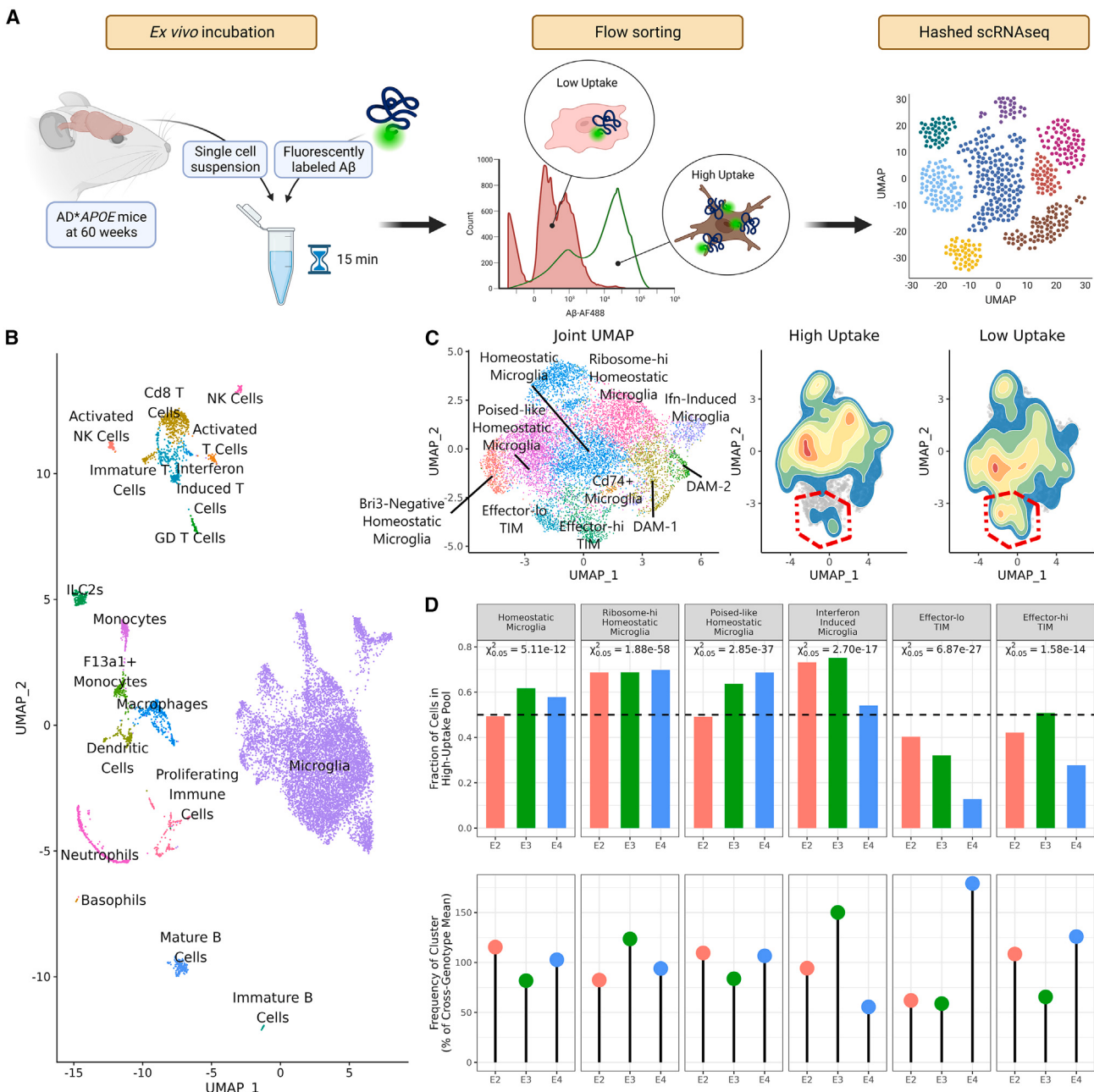


Figure 6. TIM are functionally impaired in their capacity for amyloid- β clearance

(A) Schematic of the experimental strategy to characterize microglial capacity for ex vivo A β uptake.

(B) UMAP generated from all cells sequenced after the A β uptake experiment.

(C) Joint subclustering UMAP of all microglial cells in the dataset and 2D density plots overlaid on the microglial UMAP showing cell distributions from the high uptake and low uptake populations. TIM clusters are outlined in red. Note that TIM, particularly effector-lo TIM, are depleted in the high uptake fraction.

(D) Barplot of the fraction of cells from each genotype and cluster in the high uptake pool and dotplot showing the fraction of cells from each genotype in the given cluster. Degree of over- or underrepresentation in the high uptake pool was evaluated using a chi-square test on the null expectation of an even split. p values are reported at the $\alpha = 0.05$ threshold.

DISCUSSION

Microglia display remarkable diversity, particularly within the inflammatory milieu of disease states. In this study, we present a single-cell atlas of microglial gene expression in AD in an

age- and APOE-isoform-dependent manner. Just as single-cell techniques revealed unappreciated heterogeneity in macrophage state beyond the M1-M2 paradigm,⁷⁹ these data define a microglial state beyond the homeostatic-inflammatory binary characterized by futile inflammation and impaired response to

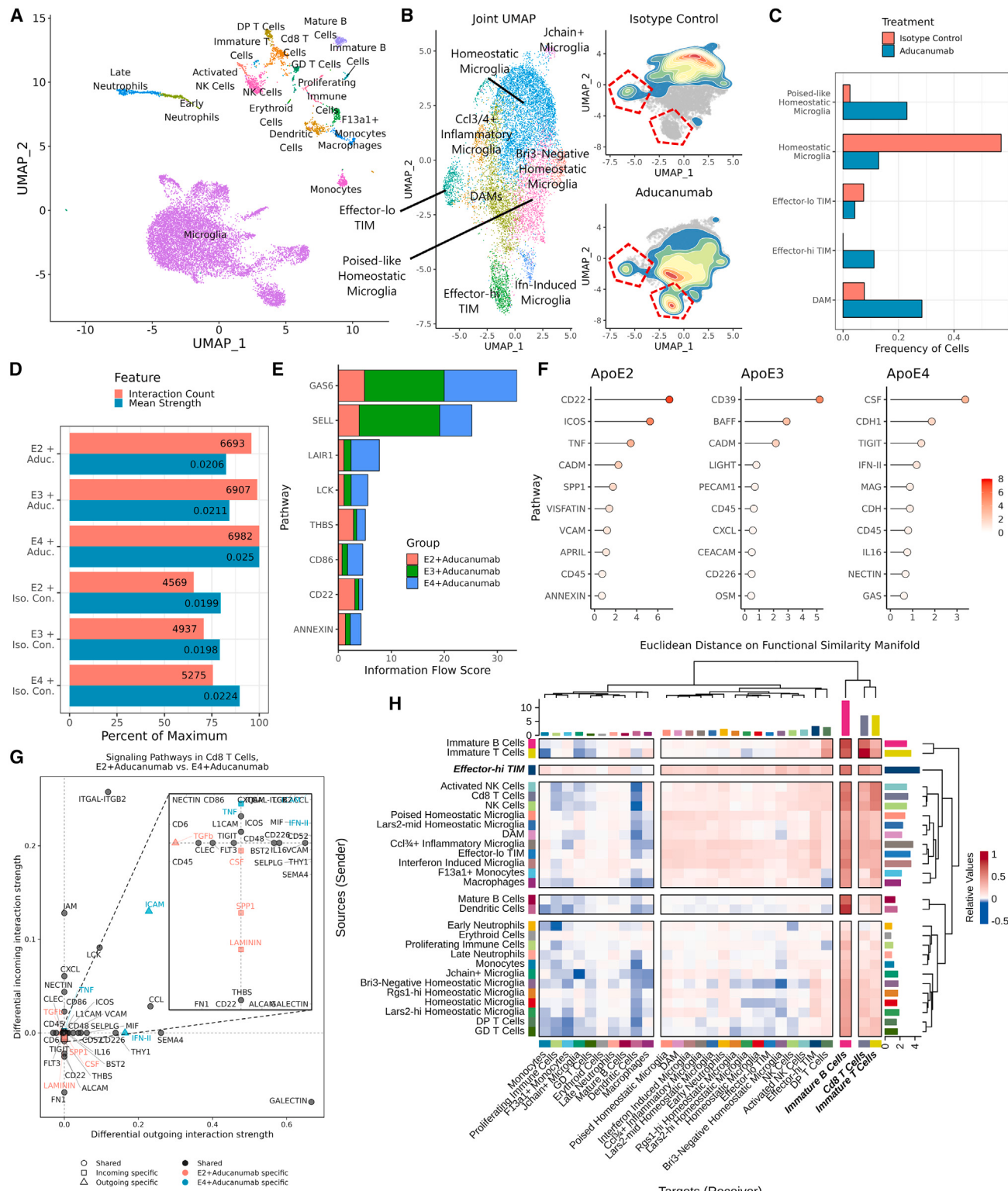


Figure 7. Aducanumab treatment profoundly alters the landscape of immune cells in the AD milieu.

Figure 7: Aducanumab treatment profoundly alters (A) LIMAP of all cells from the unified aducanumab dataset

(B) Joint subclustering UMAP of all microglial cells in the dataset and 2D density plots overlaid on the microglial UMAP showing cell distributions from the aducanumab-treated and isotype-control-treated populations. TIM clusters are outlined in red.

(C) Barplot of the frequency of microglial clusters in aducanumab-treated and isotype-control-treated populations.

(legend continued on next page)
Immunity 57, 153–170, January 9, 2024 165

chronic stimuli. We refer to this population as TIM and show that its frequency is increased by *APOE4* and age. TIM are distinguished from DAM and other previously described microglial states in several respects, including their concomitant expression of inflammatory markers and cell-intrinsic stress signatures, their distinct chromatin accessibility landscape, and their unique metabolic state and interactome.

A transcriptomic signature with some similarity to that of TIM has been presumed to represent an *ex vivo* stress signature induced by enzymatic processing.⁸⁰ However, TIM are robustly detectable in snRNA-seq datasets of human AD, irrespective of whether single-cell suspensions were prepared by enzymatic processing or cold Dounce homogenization. Although we cannot exclude enzymatic digestion as a potential confounder of transcriptional state, our analysis shows that TIM are not purely an artifact of sample preparation. Moreover, even under the interpretation that the TIM phenotype is exacerbated by *ex vivo* conditions, our data indicate that microglia from aged brains are more strongly predisposed toward stochastically adopting this state and that this transition is genetically modulated by *APOE* genotype. We consequently propose that TIM represent a bona fide microglial program and suggest that this state may have previously been underappreciated due to its age-dependent accumulation.

Many of the characteristics of TIM, most notably their decreased utilization of glycolytic pathways and their simultaneous expression of both pro- and anti-inflammatory signals, are also observed in T cell exhaustion, a phenotypic state that is similarly induced by chronic stimulation and inflammation and is marked by impaired capacity to respond to those inflammatory signals. Likewise, TIM are characterized by an elevated expression of *Serpine1*, a marker of senescence whose expression in microglia is associated with A β pathology and inflammation.⁸¹ This is further supported by the existence of a relatively minor population of TIM with a particularly high expression of *Serpine1* whose frequency is not affected by *APOE* genotype but is modified by age in the same way as other TIM states. These observations frame TIM as a potential microglial equivalent of exhausted T cells, posing the possibility that TIM represent a terminal state for activated microglia marked by a less inflammatory, functionally impaired, exhausted-like state.⁸² We note that this microglial exhaustion is distinct from microglial depletion, a chronic, systemic decrease in microglial frequency that is a suggested therapeutic strategy against AD.⁸³

In the context of the inflammatory AD milieu, these dysfunctional microglia may contribute to AD pathology, potentially explaining elements of AD evolution across stages of severity.

Moreover, the greater frequency of TIM in *APOE4* carriers may contribute to their increased susceptibility to Alzheimer's hallmarks, earlier disease onset, and differential rate of disease progression.⁸⁴ We speculate that this may occur through TIM accumulation resulting in a concomitant loss of homeostatic microglia, thereby interfering with the normal constraint of AD progression and accelerating disease pathology. Alternatively, TIM may have an active role in disruptive cell signaling or the secretion of factors that lead to detrimental disease outcomes; ligands such as IL-11, DHEA, 2-AG, and histamine, all of which were strongly enriched in TIM in our data by cell-cell interaction imputation, are worthy of further exploration in this regard.

Epidemiological studies have long noted that AD incidence is considerably higher for females than for males.⁸⁵ Although this is partially explained by the longer average lifespan of females, other factors, including post-menopausal changes in hormones and sex-specific differences in immune responses, are also implicated in this phenomenon.^{86–88} However, comparatively little is understood with respect to the putative drivers of AD that might be unique to males. One possibility is raised by a meta-analysis of the impact of herpes zoster vaccination on dementia, which revealed that although vaccination is protective against the development of dementia later in life, this effect is stronger in females than in males.⁸⁹ Our finding that TIM are enriched in males suggests a potential basis for this phenotype: the aged male neuroimmune system might be less responsive to the effects of historical immune interventions such as vaccination due to its higher burden of dysfunctional microglia. Combined with the observation that sex-specific AD risk in *APOE4* carriers is particularly exacerbated between the ages of 65 and 75 years,⁹⁰ the approximate equivalent human age range to the period in which TIM emergence is most accelerated in our murine model, we posit that TIM frequency may be a cell-type-based risk factor that partially describes the incidence and pathology of AD in males.

Our results also underscore the presence of two distinct classes of TIM in the AD milieu: effector-lo TIM are defined predominantly by stress markers, whereas effector-hi TIM maintain the expression of genes relevant to immune crosstalk and function. Although *APOE4*-bearing animals are strongly enriched for effector-lo TIM, *APOE2*-bearing animals are instead enriched for effector-hi TIM. Our functional exploration of TIM reveals that both subtypes show defects in A β clearance and that this is exacerbated in effector-lo TIM. Meanwhile, effector-hi TIM appear to be dominant contributors to the immune interactome during aducanumab treatment. Additional work is needed to clarify the differential roles of these TIM subtypes during aging,

(D) Barplot of the number of predicted interactions and the mean predicted interaction strength from each of the six samples in the aducanumab dataset, as estimated by CellChat.

(E) Stacked barplot showing the total information flow predicted by CellChat through each signaling pathway.

(F) Lollipop plot showing pathways with the highest differential regulation between aducanumab-treated and isotype-control-treated samples in each genotype, quantified by Euclidean distance on the joint functional similarity manifold produced by CellChat embedding.

(G) Dotplot of differentially enriched signaling pathways in Cd8 T cells between AD**APOE2* and AD**APOE4* aducanumab-treated animals by both incoming and outgoing signal strength. Pathways are color and shape coded by directionality and sample specificity. Positive numbers indicate a greater strength in AD**APOE4*.

(H) Heatmap showing the mean difference in incoming and outgoing signaling between aducanumab-treated and isotype-control-treated animals. Positive numbers indicate a greater strength in aducanumab-treated animals. Note that the strongest increases in outgoing signaling are in inflammatory microglia and especially in effector-hi TIM.

in AD, and at physiological steady state, as well as the mechanism by which *APOE* variants bias TIM toward different states.

Pioneering work in immunology revealed that T cells can undergo exhaustion, characterized by an increased expression of inhibitory receptors and inappropriate activation in response to a stimulus; this discovery laid the groundwork for immunotherapies that leverage antibody-based therapeutics to promote effective T cell responses.^{91,92} In much the same way, we postulate that a better understanding of the exhausted-like microglial phenotype we describe herein could enable a new treatment paradigm for AD predicated not on directly reducing neuroinflammation but instead on the reprogramming of microglia toward a more homeostatic state. Further functional characterization of TIM and their ramifications *in situ* over the course of AD pathology may therefore uncover novel regulatory nodes and therapeutic avenues for the treatment and prevention of AD.

Limitations of the study

Although the single-cell atlas generated in this work enables the exploration of deep questions in microglial heterogeneity, its statistical power is limited by the fact that one library was generated for each genotype and age. Moreover, although our analysis of human datasets identified a strong correlation between TIM frequency and sex, our murine work was underpowered with respect to this question. Future work will be necessary to validate these findings. Additionally, our computational modeling of the TIM gene regulatory network nominated a suite of AP-1 factors as being critical for either the establishment or the maintenance of the TIM state. *In vivo* studies modulating these transcription factors can conclusively determine the necessity and sufficiency of their regulation for TIM emergence. Finally, our work reveals that TIM are ubiquitous in murine and human AD, but whether TIM also play a role in non-pathological aging or other chronic neuroinflammatory conditions such as multiple sclerosis, Parkinson's disease, and brain tumors remains to be described. Computational and experimental techniques can be leveraged to explore these questions, extending our findings to microglial biology beyond the scope of AD.

STAR★METHODS

Detailed methods are provided in the online version of this paper and include the following:

- KEY RESOURCES TABLE
- RESOURCE AVAILABILITY
 - Lead contact
 - Materials availability
 - Data and code availability
- EXPERIMENTAL MODEL AND STUDY PARTICIPANT DETAILS
- METHOD DETAILS
 - Brain immune cell isolation
 - Single-cell library preparation
 - Aducanumab treatment and library preparation
 - Multiome library preparation
 - Bulk sequencing of neuroimmune cells
 - Paraffin embedded sections of human brains
 - APOE genotyping

- Xenium library preparation
 - Methoxy-X04 staining
 - Aβ uptake experiment
 - Library analysis
 - Spatial transcriptome analysis
 - Single-cell density plots
 - RNA velocity analysis
 - Ligand-receptor analysis
 - Transcription factor program analysis
 - Multiome topic modeling
 - Bulk sequencing decomposition
 - Metabolic state estimation
- QUANTIFICATION AND STATISTICAL ANALYSIS

SUPPLEMENTAL INFORMATION

Supplemental information can be found online at <https://doi.org/10.1016/j.immuni.2023.12.001>.

ACKNOWLEDGMENTS

This work was supported in part by R35CA274446 and the Reem Kayden Award. A.M. was supported by NIH T32 GM132083. We thank the Rockefeller Transgenic and Reproductive Core for assistance with IVF, the Rockefeller Genomics Core for assistance with sequencing, the Rockefeller Flow Cytometry Core for assistance with FACS, the Weill Cornell Epigenomics Core for their assistance with multiome sequencing, the Memorial Sloan Kettering Single Cell Analytics Innovation Lab for assistance with Xenium, the Memorial Sloan Kettering Molecular Cytology Core for assistance with methoxy-X04 imaging, the Rockefeller University veterinary technician team for assistance with mouse work, and Dr. Eric Hamlett for his assistance with the acquisition and preparation of human brain sections. We thank the Carroll A. Campbell, Jr. Neuropathology Laboratory at the Medical University of South Carolina for providing human brain sections. We thank Alexandra Pinzaru and King Faisal Yambire for their invaluable comments during manuscript preparation. The graphical abstract and Figures 1A, 5A, and S1B were prepared using Biorender.com.

AUTHOR CONTRIBUTIONS

J.H.L. and S.F.T. conceived the study. A.M., J.H.L., and S.F.T. supervised the study. A.M., J.H.L., and S.F.T. designed experiments. A.M. and J.H.L. performed and analyzed experiments. A.M. prepared figures. A.M., J.H.L., and S.F.T. wrote the paper.

DECLARATION OF INTERESTS

S.F.T. is a cofounder, shareholder, and member of the scientific advisory board of Inspirna.

Received: February 23, 2023

Revised: October 4, 2023

Accepted: December 4, 2023

Published: December 29, 2023

REFERENCES

1. Heneka, M.T., Carson, M.J., Khouri, J.E., Landreth, G.E., Brosseron, F., Feinstein, D.L., Jacobs, A.H., Wyss-Coray, T., Vitorica, J., Ransohoff, R.M., et al. (2015). Neuroinflammation in Alzheimer's disease. *Lancet Neurol.* 14, 388–405.
2. Long, J.M., and Holtzman, D.M. (2019). Alzheimer disease: an update on pathobiology and treatment strategies. *Cell* 179, 312–339.
3. Hansen, D.V., Hanson, J.E., and Sheng, M. (2018). Microglia in Alzheimer's disease. *J. Cell Biol.* 217, 459–472.

4. Hammond, T.R., Dufort, C., Dissing-Olesen, L., Giera, S., Young, A., Wysoker, A., Walker, A.J., Gergits, F., Segel, M., Nemesh, J., et al. (2018). Single-cell RNA sequencing of microglia throughout the mouse lifespan and in the injured brain reveals complex cell-state changes. *Immunity* 50, 253–271.e6.
5. Ginhoux, F., Greter, M., Leboeuf, M., Nandi, S., See, P., Gokhan, S., Mehler, M.F., Conway, S.J., Ng, L.G., Stanley, E.R., et al. (2010). Fate mapping analysis reveals that adult microglia derive from primitive macrophages. *Science* 330, 841–845.
6. Schulz, C., Gomez Perdiguero, E.G., Chorro, L., Szabo-Rogers, H., Cagnard, N., Kierdorf, K., Prinz, M., Wu, B., Jacobsen, S.E.W., Pollard, J.W., et al. (2012). A lineage of myeloid cells independent of Myb and hematopoietic stem cells. *Science* 336, 86–90.
7. St-Pierre, M.-K., VanderZwaag, J., Loewen, S., and Tremblay, M.-È. (2022). All roads lead to heterogeneity: the complex involvement of astrocytes and microglia in the pathogenesis of Alzheimer's disease. *Front. Cell. Neurosci.* 16, 932572.
8. Paolicelli, R.C., Sierra, A., Stevens, B., Tremblay, M.E., Aguzzi, A., Ajami, B., Amit, I., Audinat, E., Bechmann, I., Bennett, M., et al. (2022). Microglia states and nomenclature: A field at its crossroads. *Neuron* 110, 3458–3483.
9. Deczkowska, A., Keren-Shaul, H., Weiner, A., Colonna, M., Schwartz, M., and Amit, I. (2018). Disease-associated microglia: A universal immune sensor of neurodegeneration. *Cell* 173, 1073–1081.
10. Heneka, M.T., Kummer, M.P., Stutz, A., Delekate, A., Schwartz, S., Vieira-Saecker, A., Griep, A., Axt, D., Remus, A., Tzeng, T.C., et al. (2013). NLRP3 is activated in Alzheimer's disease and contributes to pathology in APP/PS1 mice. *Nature* 493, 674–678.
11. Ising, C., Venegas, C., Zhang, S., Scheiblich, H., Schmidt, S.V., Vieira-Saecker, A., Schwartz, S., Albasset, S., McManus, R.M., Tejera, D., et al. (2019). NLRP3 inflammasome activation drives tau pathology. *Nature* 575, 669–673.
12. Ennerfelt, H., Frost, E.L., Shapiro, D.A., Holliday, C., Zengeler, K.E., Voithofer, G., Bolte, A.C., Lammert, C.R., Kulas, J.A., Ulland, T.K., et al. (2022). SYK coordinates neuroprotective microglial responses in neurodegenerative disease. *Cell* 185, 4135–4152.e22.
13. Wang, S., Sudan, R., Peng, V., Zhou, Y., Du, S., Yuede, C.M., Lei, T., Hou, J., Cai, Z., Cella, M., et al. (2022). TREM2 drives microglia response to amyloid- β via SYK-dependent and -independent pathways. *Cell* 185, 4153–4169.e19.
14. Sierra, A., Abiega, O., Shahraz, A., and Neumann, H. (2013). Janus-faced microglia: beneficial and detrimental consequences of microglial phagocytosis. *Front. Cell. Neurosci.* 7, 6.
15. Khalil, Y.A., Rabès, J.-P., Boileau, C., and Varret, M. (2021). APOE gene variants in primary dyslipidemia. *Atherosclerosis* 328, 11–22.
16. Liu, C.-C., Liu, C.-C., Kanekiyo, T., Xu, H., and Bu, G. (2013). Apolipoprotein E and Alzheimer disease: risk, mechanisms and therapy. *Nat. Rev. Neurol.* 9, 106–118.
17. Tavazoie, M.F., Pollack, I., Tanqueco, R., Ostendorf, B.N., Reis, B.S., Gonsalves, F.C., Kurth, I., Andreu-Agullo, C., Derbyshire, M.L., Posada, J., et al. (2018). LXR/ApoE activation restricts innate immune suppression in cancer. *Cell* 172, 825–840.e18.
18. Ostendorf, B.N., Bilanovic, J., Adaku, N., Tafreshian, K.N., Tavora, B., Vaughan, R.D., and Tavazoie, S.F. (2020). Common germline variants of the human APOE gene modulate melanoma progression and survival. *Nat. Med.* 26, 1048–1053.
19. Ostendorf, B.N., Patel, M.A., Bilanovic, J., Hoffmann, H.-H., Carrasco, S.E., Rice, C.M., and Tavazoie, S.F. (2022). Common human genetic variants of APOE impact murine COVID-19 mortality. *Nature* 611, 346–351.
20. Shi, Y., Yamada, K., Liddelow, S.A., Smith, S.T., Zhao, L., Luo, W., Tsai, R.M., Spina, S., Grinberg, L.T., Rojas, J.C., et al. (2017). Initiative, A.D.N. *Nature* 549, 523–527.
21. Roussarie, J.-P., Yao, V., Rodriguez-Rodriguez, P., Oughtred, R., Rust, J., Plautz, Z., Kasturia, S., Albornoz, C., Wang, W., Schmidt, E.F., et al. (2020). Selective neuronal vulnerability in Alzheimer's disease: A network-based analysis. *Neuron* 107, 821–835.e12.
22. Tziaras, M., McGeachan, R.I., Durrant, C.S., and Spires-Jones, T.L. (2023). Synaptic degeneration in Alzheimer disease. *Nat. Rev. Neurol.* 19, 19–38.
23. Bero, A.W., Yan, P., Roh, J.H., Cirrito, J.R., Stewart, F.R., Raichle, M.E., Lee, J.M., and Holtzman, D.M. (2011). Neuronal activity regulates the regional vulnerability to amyloid- β deposition. *Nat. Neurosci.* 14, 750–756.
24. Stuart, T., Butler, A., Hoffman, P., Hafemeister, C., Papalexi, E., Mauck, W.M., Hao, Y., Stoeckius, M., Smibert, P., and Satija, R. (2019). Comprehensive integration of single-cell data. *Cell* 177, 1888–1902.e21.
25. Keren-Shaul, H., Spinrad, A., Weiner, A., Matcovitch-Natan, O., Dvir-Sternfeld, R., Ulland, T.K., David, E., Baruch, K., Lara-Astaiso, D., Toth, B., et al. (2017). A unique microglia type associated with restricting development of Alzheimer's disease. *Cell* 179, 1276–1290.e17.
26. Lubatti, G., Stock, M., Iturbide, A., Segura, M.L.R.T., Tyser, R., Theis, F.J., Srinivas, S., Torres-Padilla, M.-E., and Scialdone, A. (2022). CIARA: a cluster-independent algorithm for the identification of markers of rare cell types from single-cell RNA seq data. <https://doi.org/10.1101/2022.08.01.501965>.
27. Law, C.W., Chen, Y., Shi, W., and Smyth, G.K. (2014). voom: precision weights unlock linear model analysis tools for RNA-seq read counts. *Genome Biol.* 15, R29.
28. Hippen, A.A., Falco, M.M., Weber, L.M., Erkan, E.P., Zhang, K., Doherty, J.A., Vähärautio, A., Greene, C.S., and Hicks, S.C. (2021). miQC: an adaptive probabilistic framework for quality control of single-cell RNA-sequencing data. *PLoS Comput. Biol.* 17, e1009290.
29. Onuska, K.M. (2020). The dual role of microglia in the progression of Alzheimer's disease. *J. Neurosci.* 40, 1608–1610.
30. Melsted, P., Booshagh, A.S., Liu, L., Gao, F., Lu, L., Min, K.H. (Joseph), Beltrame, E.d.V., Hjörleifsson, K.E., Gehring, J., and Pachter, L. (2021). Modular, efficient and constant-memory single-cell RNA-seq preprocessing. *Nat. Biotechnol.* 39, 813–818.
31. Lange, M., Bergen, V., Klein, M., Setty, M., Reuter, B., Bakhti, M., Lickert, H., Ansari, M., Schniering, J., Schiller, H.B., et al. (2022). CellRank for directed single-cell fate mapping. *Nat. Methods* 19, 159–170.
32. Gulati, G.S., Sikandar, S.S., Wesche, D.J., Manjunath, A., Bharadwaj, A., Berger, M.J., Ilagan, F., Kuo, A.H., Hsieh, R.W., Cai, S., et al. (2020). Single-cell transcriptional diversity is a hallmark of developmental potential. *Science* 367, 405–411.
33. Jew, B., Alvarez, M., Rahmani, E., Miao, Z., Ko, A., Garske, K.M., Sul, J.H., Pietiläinen, K.H., Pajukanta, P., and Halperin, E. (2020). Accurate estimation of cell composition in bulk expression through robust integration of single-cell information. *Nat. Commun.* 11, 1971.
34. Abar, S., González-Blas, C.B., Moerman, T., Huynh-Thu, V.A., Imrichova, H., Hulselmans, G., Rambow, F., Marine, J.-C., Geurts, P., Aerts, J., et al. (2017). SCENIC: single-cell regulatory network inference and clustering. *Nat. Methods* 14, 1083–1086.
35. Honda, K., Yanai, H., Negishi, H., Asagiri, M., Sato, M., Mizutani, T., Shimada, N., Ohba, Y., Takaoka, A., Yoshida, N., et al. (2005). IRF-7 is the master regulator of type-I interferon-dependent immune responses. *Nature* 434, 772–777.
36. Grubman, A., Choo, X.Y., Chew, G., Ouyang, J.F., Sun, G., Croft, N.P., Rossello, F.J., Simmons, R., Buckberry, S., Landin, D.V., et al. (2021). Transcriptional signature in microglia associated with A β plaque phagocytosis. *Nat. Commun.* 12, 3015.
37. Brioschi, S., Belk, J.A., Peng, V., Molgora, M., Rodrigues, P.F., Nguyen, K.M., Wang, S., Du, S., Wang, W.-L., Grajales-Reyes, G.E., et al. (2023). A Cre-deleter specific for embryo-derived brain macrophages reveals distinct features of microglia and border macrophages. *Immunity* 56, 1027–1045.e8.

38. Wang, C., Fan, L., Khawaja, R.R., Liu, B., Zhan, L., Kodama, L., Chin, M., Li, Y., Le, D., Zhou, Y., et al. (2022). Microglial NF- κ B drives tau spreading and toxicity in a mouse model of tauopathy. *Nat. Commun.* **13**, 1969.
39. Liu, T., Zhu, B., Liu, Y., Zhang, X., Yin, J., Li, X., Jiang, L., Hodges, A.P., Rosenthal, S.B., Zhou, L., et al. (2020). Multi-omic comparison of Alzheimer's variants in human ESC-derived microglia reveals convergence at APOE. *J. Exp. Med.* **217**, e20200474.
40. Efremova, M., Vento-Tormo, M., Teichmann, S.A., and Vento-Tormo, R. (2020). CellPhoneDB: inferring cell-cell communication from combined expression of multi-subunit ligand-receptor complexes. *Nat. Protoc.* **15**, 1484–1506.
41. Maheshwari, A., Janssens, K., Bogie, J., Haute, C.V.D., Struys, T., Lambrechts, I., Baekelandt, V., Stinissen, P., Hendriks, J.J.A., Slaets, H., et al. (2013). Local overexpression of interleukin-11 in the central nervous system limits demyelination and enhances remyelination. *Medit. Inflam.* **2013**, 685317.
42. Alexaki, V.I., Fodelianaki, G., Neuwirth, A., Mund, C., Kouriantaki, A., Ieronimaki, E., Lyroni, K., Troullinaki, M., Fujii, C., Kanczkowski, W., et al. (2018). DHEA inhibits acute microglia-mediated inflammation through activation of the TrkA-Akt1/2-CREB-Jmjd3 pathway. *Mol. Psychiatry* **23**, 1410–1420.
43. Mecha, M., Yanguas-Casás, N., Feliú, A., Mestre, L., Carrillo-Salinas, F., Azcoitia, I., Yong, V.W., and Guaza, C. (2019). The endocannabinoid 2-AG enhances spontaneous remyelination by targeting microglia. *Brain Behav. Immun.* **77**, 110–126.
44. Zhang, D., Hu, X., Qian, L., Chen, S.-H., Zhou, H., Wilson, B., Miller, D.S., and Hong, J.-S. (2011). Microglial MAC1 receptor and PI3K are essential in mediating β -amyloid peptide-induced microglial activation and subsequent neurotoxicity. *J. Neuroinflammation* **8**, 3.
45. Gao, H.-M., Zhou, H., Zhang, F., Wilson, B.C., Kam, W., and Hong, J.-S. (2011). HMGB1 acts on microglia Mac1 to mediate chronic neuroinflammation that drives progressive neurodegeneration. *J. Neurosci.* **31**, 1081–1092.
46. Hijikata, M., Futokoro, R., Ohto-Nakanishi, T., Nakanishi, H., Katsuki, H., and Kitamura, Y. (2020). Microglia-released leukotriene B4 promotes neutrophil infiltration and microglial activation following intracerebral hemorrhage. *Int. Immunopharmacol.* **85**, 106678.
47. Spittau, B., Dokalis, N., and Prinz, M. (2020). The role of TGF β signaling in microglia maturation and activation. *Trends Immunol.* **41**, 836–848.
48. Fansler, M.M., Zhen, G., and Mayr, C. (2021). Quantification of alternative 3'UTR isoforms from single cell RNA-seq data with scUTRquant. <https://doi.org/10.1101/2021.11.22.469635>.
49. Wagner, A., Wang, C., Fessler, J., DeTomaso, D., Avila-Pacheco, J., Kaminski, J., Zaghouani, S., Christian, E., Thakore, P., Schellhaass, B., et al. (2021). Metabolic modeling of single Th17 cells reveals regulators of autoimmunity. *Cell* **184**, 4168–4185.e21.
50. Stuart, T., Srivastava, A., Madad, S., Lareau, C.A., and Satija, R. (2021). Single-cell chromatin state analysis with Signac. *Nat. Methods* **18**, 1333–1341.
51. Schep, A.N., Wu, B., Buenrostro, J.D., and Greenleaf, W.J. (2017). chromVAR: inferring transcription-factor-associated accessibility from single-cell epigenomic data. *Nat. Methods* **14**, 975–978.
52. Lynch, A.W., Theodoris, C.V., Long, H.W., Brown, M., Liu, X.S., and Meyer, C.A. (2022). MIRA: joint regulatory modeling of multimodal expression and chromatin accessibility in single cells. *Nat. Methods* **19**, 1097–1108.
53. González-Blas, C.B., Winter, S.D., Hulselmans, G., Hecker, N., Matetovici, I., Christiaens, V., Poovathingal, S., Wouters, J., Aibar, S., and Aerts, S. (2023). SCENIC+: single-cell multiomic inference of enhancers and gene regulatory networks. *Nat. Methods* **20**, 1355–1367.
54. Zhang, W., Zhang, X., Zhang, Y., Qu, C., Zhou, X., and Zhang, S. (2020). Histamine induces microglia activation and the release of proinflammatory mediators in rat brain via H1R or H4R. *J. Neuroimmune Pharmacol.* **15**, 280–291.
55. Ferreira, R., Santos, T., Gonçalves, J., Baltazar, G., Ferreira, L., Agasse, F., and Bernardino, L. (2012). Histamine modulates microglia function. *J. Neuroinflammation* **9**, 90.
56. Olah, M., Menon, V., Habib, N., Taga, M.F., Ma, Y., Yung, C.J., Cimpean, M., Khairallah, A., Coronas-Samano, G., Sankowski, R., et al. (2020). Single cell RNA sequencing of human microglia uncovers a subset associated with Alzheimer's disease. *Nat. Commun.* **11**, 6129.
57. Blanchard, J.W., Akay, L.A., Davila-Velderrain, J., Maydell, D. von, Mathys, H., Davidson, S.M., Effenberger, A., Chen, C.-Y., Maner-Smith, K., Hajjar, I., et al. (2022). APOE impairs myelination via cholesterol dysregulation in oligodendrocytes. *Nature* **611**, 769–779.
58. Mathys, H., Davila-Velderrain, J., Peng, Z., Gao, F., Mohammadi, S., Young, J.Z., Menon, M., He, L., Abdurrob, F., Jiang, X., et al. (2019). Single-cell transcriptomic analysis of Alzheimer's disease. *Nature* **570**, 332–337.
59. Morabito, S., Miyoshi, E., Michael, N., Shahin, S., Martini, A.C., Head, E., Silva, J., Leavy, K., Perez-Rosendahl, M., and Swarup, V. (2021). Single-nucleus chromatin accessibility and transcriptomic characterization of Alzheimer's disease. *Nat. Genet.* **53**, 1143–1155.
60. Lau, S.-F., Cao, H., Fu, A.K.Y., and Ip, N.Y. (2020). Single-nucleus transcriptome analysis reveals dysregulation of angiogenic endothelial cells and neuroprotective glia in Alzheimer's disease. *Proc. Natl. Acad. Sci. USA* **117**, 25800–25809.
61. Leng, K., Li, E., Eser, R., Piergies, A., Sit, R., Tan, M., Neff, N., Li, S.H., Rodriguez, R.D., Sueamoto, C.K., et al. (2021). Molecular characterization of selectively vulnerable neurons in Alzheimer's disease. *Nat. Neurosci.* **24**, 276–287.
62. Grubman, A., Chew, G., Ouyang, J.F., Sun, G., Choo, X.Y., McLean, C., Simmons, R.K., Buckberry, S., Vargas-Landin, D.B., Poppe, D., et al. (2019). A single-cell atlas of entorhinal cortex from individuals with Alzheimer's disease reveals cell-type-specific gene expression regulation. *Nat. Neurosci.* **22**, 2087–2097.
63. Gabitto, M.I., Travaglini, K.J., Rachleff, V.M., Kaplan, E.S., Long, B., Ariza, J., Ding, Y., Mahoney, J.T., Dee, N., Goldy, J., et al. (2023). Integrated multimodal cell atlas of Alzheimer's disease. <https://doi.org/10.1101/2023.05.08.539485>.
64. Green, G.S., Fujita, M., Yang, H.-S., Taga, M., McCabe, C., Cain, A., White, C.C., Schmidtner, A.K., Zeng, L., Wang, Y., et al. (2023). Cellular dynamics across aged human brains uncover a multicellular cascade leading to Alzheimer's disease. <https://doi.org/10.1101/2023.03.07.531493>.
65. Cain, A., Taga, M., McCabe, C., Green, G.S., Hekselman, I., White, C.C., Lee, D.I., Gaur, P., Rozenblatt-Rosen, O., Zhang, F., et al. (2023). Multicellular communities are perturbed in the aging human brain and Alzheimer's disease. *Nat. Neurosci.* **26**, 1267–1280.
66. Prater, K.E., Green, K.J., Mamde, S., Sun, W., Cochoit, A., Smith, C.L., Chiou, K.L., Heath, L., Rose, S.E., Wiley, J., et al. (2023). Human microglia show unique transcriptional changes in Alzheimer's disease. *Nat. Aging* **3**, 894–907.
67. Consortium, T.T.M., Almanzar, N., Antony, J., Baghel, A.S., Bakerman, I., Bansal, I., Barres, B.A., Beachy, P.A., Berdnik, D., Bilen, B., et al. (2020). A single-cell transcriptomic atlas characterizes ageing tissues in the mouse. *Nature* **583**, 590–595.
68. Palla, G., Spitzer, H., Klein, M., Fischer, D., Schaer, A.C., Kuemmerle, L.B., Rybakov, S., Ibarra, I.L., Holmberg, O., Virshup, I., et al. (2022). Squidpy: a scalable framework for spatial omics analysis. *Nat. Methods* **19**, 171–178.
69. Sevigny, J., Chiao, P., Bussière, T., Weinreb, P.H., Williams, L., Maier, M., Dunstan, R., Salloway, S., Chen, T., Ling, Y., et al. (2016). The antibody aducanumab reduces A β plaques in Alzheimer's disease. *Nature* **537**, 50–56.
70. Budd, Haeberlein, S.B., Aisen, P.S., Barkhof, F., Chalkias, S., Chen, T., Cohen, S., Dent, G., Hansson, O., Harrison, K., Hehn, C. von, et al. (2022). Two randomized Phase 3 studies of aducanumab in early Alzheimer's disease. *J. Prev. Alzheimer's Dis.* **9**, 197–210.

71. Jin, S., Guerrero-Juarez, C.F., Zhang, L., Chang, I., Ramos, R., Kuan, C.-H., Myung, P., Plikus, M.V., and Nie, Q. (2021). Inference and analysis of cell-cell communication using CellChat. *Nat. Commun.* 12, 1088.
72. Owlett, L.D., Karaahmet, B., Le, L., Belcher, E.K., Dionisio-Santos, D., Olschowka, J.A., Elliott, M.R., and O'Banion, M.K. (2022). Gas6 induces inflammation and reduces plaque burden but worsens behavior in a sex-dependent manner in the APP/PS1 model of Alzheimer's disease. *J. Neuroinflammation* 19, 38.
73. Pluvinage, J.V., Haney, M.S., Smith, B.A.H., Sun, J., Iram, T., Bonanno, L., Li, L., Lee, D.P., Morgens, D.W., Yang, A.C., et al. (2019). CD22 blockade restores homeostatic microglial phagocytosis in aging brains. *Nature* 568, 187–192.
74. Matyash, M., Zabiegalov, O., Wendt, S., Matyash, V., and Kettenmann, H. (2017). The adenosine generating enzymes CD39/CD73 control microglial processes ramification in the mouse brain. *PLoS One* 12, e0175012.
75. Elmore, M.R.P., Najafi, A.R., Koike, M.A., Dagher, N.N., Spangenberg, E.E., Rice, R.A., Kitazawa, M., Matusow, B., Nguyen, H., West, B.L., et al. (2014). Colony-stimulating Factor 1 receptor signaling is necessary for microglia viability, unmasking a microglia progenitor cell in the adult brain. *Neuron* 82, 380–397.
76. Louveau, A., Smirnov, I., Keyes, T.J., Eccles, J.D., Rouhani, S.J., Peske, J.D., Derecki, N.C., Castle, D., Mandell, J.W., Lee, K.S., et al. (2015). Structural and functional features of central nervous system lymphatic vessels. *Nature* 523, 337–341.
77. Da Mesquita, S.D., Louveau, A., Vaccari, A., Smirnov, I., Cornelison, R.C., Kingsmore, K.M., Contarino, C., Onengut-Gumuscu, S., Farber, E., Raper, D., et al. (2018). Functional aspects of meningeal lymphatics in aging and Alzheimer's disease. *Nature* 560, 185–191.
78. Schafflick, D., Wolbert, J., Heming, M., Thomas, C., Hartlehnert, M., Börsch, A.-L., Ricci, A., Martín-Salamanca, S., Li, X., Lu, I.-N., et al. (2021). Single-cell profiling of CNS border compartment leukocytes reveals that B cells and their progenitors reside in non-diseased meninges. *Nat. Neurosci.* 24, 1225–1234.
79. Ma, R.-Y., Black, A., and Qian, B.-Z. (2022). Macrophage diversity in cancer revisited in the era of single-cell omics. *Trends Immunol.* 43, 546–563.
80. Marsh, S.E., Walker, A.J., Kamath, T., Dissing-Olesen, L., Hammond, T.R., Soysa, T.Y. de, Young, A.M.H., Murphy, S., Abdulraouf, A., Nadaf, N., et al. (2022). Dissection of artificial and confounding glial signatures by single-cell sequencing of mouse and human brain. *Nat. Neurosci.* 25, 306–316.
81. Hu, Y., Fryatt, G.L., Ghorbani, M., Obst, J., Menassa, D.A., Martin-Estebane, M., Muntslag, T.A.O., Olmos-Alonso, A., Guerrero-Carrasco, M., Thomas, D., et al. (2021). Replicative senescence dictates the emergence of disease-associated microglia and contributes to A β pathology. *Cell Rep.* 35, 109228.
82. Kummer, M.P., Ising, C., Kummer, C., Sarlus, H., Griepl, A., Vieira-Saecker, A., Schwartz, S., Halle, A., Brückner, M., Händler, K., et al. (2021). Microglial PD-1 stimulation by astrocytic PD-L1 suppresses neuroinflammation and Alzheimer's disease pathology. *EMBO J.* 40, e108662.
83. Spangenberg, E., Severson, P.L., Hohsfield, L.A., Crapser, J., Zhang, J., Burton, E.A., Zhang, Y., Spevak, W., Lin, J., Phan, N.Y., et al. (2019). Sustained microglial depletion with CSF1R inhibitor impairs parenchymal plaque development in an Alzheimer's disease model. *Nat. Commun.* 10, 3758.
84. Sando, S.B., Melquist, S., Cannon, A., Hutton, M.L., Sletvold, O., Saltvedt, I., White, L.R., Lydersen, S., and Aasly, J.O. (2008). APOE ϵ 4 lowers age at onset and is a high risk factor for Alzheimer's disease; a case control study from central Norway. *BMC Neurol.* 8, 9.
85. Seshadri, S., Wolf, P.A., Beiser, A., Au, R., McNulty, K., White, R., and D'Agostino, R.B. (1997). Lifetime risk of dementia and Alzheimer's disease: the impact of mortality on risk estimates in the Framingham study. *Neurology* 49, 1498–1504.
86. Coales, I., Tsartsalis, S., Fancy, N., Weinert, M., Clode, D., Owen, D., and Matthews, P.M. (2022). Alzheimer's disease-related transcriptional sex differences in myeloid cells. *J. Neuroinflammation* 19, 247.
87. Klein, S.L., and Flanagan, K.L. (2016). Sex differences in immune responses. *Nat. Rev. Immunol.* 16, 626–638.
88. Xiong, J., Kang, S.S., Wang, Z., Liu, X., Kuo, T.-C., Korkmaz, F., Padilla, A., Miyashita, S., Chan, P., Zhang, Z., et al. (2022). FSH blockade improves cognition in mice with Alzheimer's disease. *Nature* 603, 470–476.
89. Eying, M., Xie, M., Heß, S., Heß, S., and Geldsetzer, P. (2023). Causal evidence that herpes zoster vaccination prevents a proportion of dementia cases. <https://doi.org/10.1101/2023.05.23.23290253>.
90. Neu, S.C., Pa, J., Kukull, W., Beekly, D., Kuzma, A., Gangadharan, P., Wang, L.S., Romero, K., Arneric, S.P., Redolfi, A., et al. (2017). Apolipoprotein E genotype and sex risk factors for Alzheimer disease: A meta-analysis. *JAMA Neurol.* 74, 1178–1189.
91. Barber, D.L., Wherry, E.J., Masopust, D., Zhu, B., Allison, J.P., Sharpe, A.H., Freeman, G.J., and Ahmed, R. (2006). Restoring function in exhausted CD8 T cells during chronic viral infection. *Nature* 439, 682–687.
92. Leach, D.R., Krummel, M.F., and Allison, J.P. (1996). Enhancement of antitumor immunity by CTLA-4 blockade. *Science* 271, 1734–1736.
93. Hao, Y., Hao, S., Andersen-Nissen, E., Mauck, W.M., Zheng, S., Butler, A., Lee, M.J., Wilk, A.J., Darby, C., Zager, M., et al. (2021). Integrated analysis of multimodal single-cell data. *Cell* 184, 3573–3587.e29.
94. Zhang, Y., Liu, T., Meyer, C.A., Eeckhoute, J., Johnson, D.S., Bernstein, B.E., Nusbaum, C., Myers, R.M., Brown, M., Li, W., et al. (2008). Model-based analysis of ChIP-seq (MACS). *Genome Biol.* 9, R137.
95. Bergen, V., Lange, M., Peidli, S., Wolf, F.A., and Theis, F.J. (2020). Generalizing RNA velocity to transient cell states through dynamical modeling. *Nat. Biotechnol.* 38, 1408–1414.
96. Patro, R., Duggal, G., Love, M.I., Irizarry, R.A., and Kingsford, C. (2017). Salmon provides fast and bias-aware quantification of transcript expression. *Nat. Methods* 14, 417–419.
97. Ledo, J.H., Zhang, R., Mesin, L., Mourão-Sá, D., Azevedo, E.P., Troyanskaya, O.G., Bustos, V., and Greengard, P. (2020). Lack of a site-specific phosphorylation of presenilin 1 disrupts microglial gene networks and progenitors during development. *PLoS One* 15, e023773.
98. Mass, E., Jacome-Galarza, C.E., Blank, T., Lazarov, T., Durham, B.H., Ozkaya, N., Pastore, A., Schwabenland, M., Chung, Y.R., Rosenblum, M.K., et al. (2017). A somatic mutation in erythro-myeloid progenitors causes neurodegenerative disease. *Nature* 549, 389–393.
99. Parkhurst, C.N., Yang, G., Ninan, I., Savas, J.N., Yates, J.R., Lafaille, J.J., Hempstead, B.L., Littman, D.R., and Gan, W.-B. (2013). Microglia promote learning-dependent synapse formation through brain-derived neurotrophic factor. *Cell* 155, 1596–1609.
100. Garré, J.M., Silva, H.M., Lafaille, J.J., and Yang, G. (2017). CX3CR1+ monocytes modulate learning and learning-dependent dendritic spine remodeling via TNF- α . *Nat. Med.* 23, 714–722.
101. Stoeckius, M., Zheng, S., Houck-Loomis, B., Hao, S., Yeung, B.Z., Mauck, W.M., Smibert, P., and Satija, R. (2018). Cell Hashing with bar-coded antibodies enables multiplexing and doublet detection for single cell genomics. *Genome Biol.* 19, 224.
102. Sadeghi, H.M., Sabzghabaee, A.M., Mousavian, Z., Saadatnia, M., Shirani, S., and Moazen, F. (2011). Polymorphism of Apo lipoprotein E gene and the risk of multiple sclerosis. *J. Res. Med. Sci.* 16, 1519–1524.
103. Ledo, J.H., Liebmann, T., Zhang, R., Chang, J.C., Azevedo, E.P., Wong, E., Silva, H.M., Troyanskaya, O.G., Bustos, V., and Greengard, P. (2020). Presenilin 1 phosphorylation regulates amyloid- β degradation by microglia. *Mol. Psychiatry*, 1–16.

STAR★METHODS

KEY RESOURCES TABLE

REAGENT or RESOURCE	SOURCE	IDENTIFIER
Antibodies		
TruStain FcX	BioLegend	Cat#101319; RRID:AB_1574975
Alexa Fluor® 700 anti-mouse CD45 Antibody	BioLegend	Cat#103127; RRID:AB_493715
TotalSeq™-C0302 anti-mouse Hashtag 2 Antibody	BioLegend	Cat#155863; RRID:AB_2800694
TotalSeq™-C0303 anti-mouse Hashtag 3 Antibody	BioLegend	Cat#155865; RRID:AB_2800695
TotalSeq™-C0304 anti-mouse Hashtag 4 Antibody	BioLegend	Cat#155867; RRID:AB_2800696
TotalSeq™-C0305 anti-mouse Hashtag 5 Antibody	BioLegend	Cat#155869; RRID:AB_2800697
TotalSeq™-C0306 anti-mouse Hashtag 6 Antibody	BioLegend	Cat#155871; RRID:AB_2819910
TotalSeq™-C0308 anti-mouse Hashtag 8 Antibody	BioLegend	Cat#155875; RRID:AB_2819912
Biological Samples		
Brain sections from postmortem human AD donors	This paper	N/A
Chemicals, Peptides, and Recombinant Proteins		
Collagenase D	Roche	Cat#11088858001
Percoll	Sigma	Cat#P1644-100ML
DAPI	Sigma	Cat#D8417-1MG
40um Strainer	Flowmi	Cat#BAH136800040-50EA
Aducanumab	Cardinal Health	Cat#64406-0101-01
Human IgG Isotype Control	Invitrogen	Cat#02-7102
Sigma Protector RNase Inhibitor	Sigma	Cat#3335402001
Buffer RLT	QIAGEN	Cat#79216
AflII	New England Biolabs	Cat#R0520S
Haell	New England Biolabs	Cat#R0107S
Human Brain Gene Expression Panel	10X Genomics	Cat#1000599
Methoxy-X04	Tocris Bioscience	Cat#4920
SYTOX Green	ThermoFischer	Cat#S7020
Aβ 1-42, HiLexa™ Fluor 488-labeled	Anaspec	Cat#AS-65627
Critical Commercial Assays		
RNeasy Micro Kit	QIAGEN	Cat#74004
SMART-Seq v4 Low Input Kit	Takara Bio	Cat#634894
E.Z. 96 Tissue DNA Kit	Omega Bio-Tek	Cat#D1196-00
Deposited Data		
Raw data, Cell Ranger outputs, and processed Seurat and Signac structures for atlas and multiome dataset	This paper	GEO: GSE225503
Raw data, Cell Ranger outputs, and processed Seurat and structures for aducanumab experiments	This paper	GEO: GSE239975
Raw data, Cell Ranger outputs, and processed Seurat and structures for Aβ uptake experiments	This paper	GEO: GSE239974
Raw data and counts matrices from bulk sequencing of aged AD*APOE mice	This paper	GEO: GSE239977
Xenium raw data, processed Squidpy structure, and full-slide scans from methoxy-X04 imaging	This paper	https://10.5281/zenodo.8206638
Data from Blanchard et al. ⁵⁷	Synapse	syn38120890
Data from Mathys et al. ⁵⁸	Synapse	syn18485175
Data from Morabito et al. ⁵⁹	Synapse	syn22079621
Data from Lau et al. ⁶⁰	GEO	GSE157827
Data from Leng et al. ⁶¹	Synapse	syn21788402

(Continued on next page)

Continued

REAGENT or RESOURCE	SOURCE	IDENTIFIER
Data from Grubman et al. ⁶²	GEO	GSE138852
Data from Gabitto et al. ⁶³	brain-map.org	UMSVXTDIAZTAFKGE43T
Data from Prater et al. ⁶⁶	Synapse	syn51272688
ROSMAP DLPFC-1 (Data from Green et al. ⁶⁴)	Synapse	syn16780177
ROSMAP DLPFC-2 (Data from Cain et al. ⁶⁵)	Synapse	syn31512863
Experimental Models: Organisms/Strains		
C57BL/6	Jackson Laboratory	Cat#000664
5×FAD	Jackson Laboratory	Cat#34840
B6.129P2-Apoe ^{tm1(APOE*2)Mae} N9	Taconic Biosciences	Cat#1547
B6.129P2-Apoe ^{tm2(APOE*3)Mae} N8	Taconic Biosciences	Cat#1548
B6.129P2-Apoe ^{tm3(APOE*4)Mae} N8	Taconic Biosciences	Cat#1549
Oligonucleotides		
APOE F: ACAGAATTGCCCGGCCTGGTACAC	IDT	N/A
APOE R: TAAGCTTGGCACGGCTGTCCAAGGA	IDT	N/A
Software and Algorithms		
Analysis scripts	This paper	https://github.com/alonmillet/apoe-ad-age-atlas
R 4.1	R Foundation for Statistical Computing	RRID:SCR_001905
Python 3.7	Python Software Foundation	RRID:SCR_008394
FlowJo	Tree Star	RRID:SCR_008520
ILOG CPLEX Optimization Studio	IBM	N/A
CellRanger	10X Genomics	RRID:SCR_023221
Seurat	Hao et al. ⁹³	RRID:SCR_007322
miQC	Hippen et al. ²⁸	RRID:SCR_022697
MACS2	Zhang et al. ⁹⁴	RRID:SCR_013291
Squidpy	Palla et al. ⁶⁸	N/A
kb-python	Melsted et al. ³⁰	RRID:SCR_018213
scVelo	Bergen et al. ⁹⁵	RRID:SCR_018168
CellRank	Lange et al. ³¹	RRID:SCR_022827
CytoTRACE	Gulati et al. ³²	RRID:SCR_022828
CellPhoneDB	Efremova et al. ⁴⁰	RRID:SCR_017054
CellChat	Jin et al. ⁷¹	RRID:SCR_021946
SCENIC	Aibar et al. ³⁴	RRID:SCR_017247
SCENIC+	González-Blas et al. ⁵³	N/A
MIRA	Lynch et al. ⁵²	N/A
Bisque	Jew et al. ³³	N/A
Salmon	Patro et al. ⁹⁶	RRID:SCR_017036
Compass	Wagner et al. ⁴⁹	N/A

RESOURCE AVAILABILITY**Lead contact**

Further information and requests for resources and reagents should be directed to and will be fulfilled by the lead contact, Sohail Tavazoie (sohail.tavazoie@rockefeller.edu).

Materials availability

The AD⁺APOE mouse lines generated in this study will be made available for academic use upon reasonable request.

Data and code availability

- Collectively, all new sequencing data generated in this study are available on GEO under SuperSeries GSE239999. All raw data, Cell Ranger outputs, and processed Seurat and Signac structures for the atlas and multiome dataset are available on GEO under accession number GSE225503. All raw data, Cell Ranger outputs, and processed Seurat structures for the aducanumab treatment experiments are available on GEO under accession number GSE239975. All raw data, Cell Ranger outputs, and processed Seurat structures for the A β uptake experiments are available on GEO under accession number GSE239974. All raw data and counts matrices from bulk sequencing of aged AD*APOE mice are available on GEO under accession number GSE239977. All Xenium raw data, the processed Squidpy structure, and full-slide scans after post-Xenium methoxy-X04 staining are available on Zenodo at <https://doi.org/10.5281/zenodo.8206638>. The ROSMAP DLPFC-1 and DLPFC-2 data used in this analysis are available at Synapse under accession codes syn16780177 and syn31512863.
- All R and Python code necessary to reproduce the analysis and figures in this manuscript has been annotated and uploaded to GitHub at <https://github.com/alonmillet/apoe-ad-age-atlas>.
- Any additional information required to reanalyze the data reported in this paper is available from the [lead contact](#) upon request.

EXPERIMENTAL MODEL AND STUDY PARTICIPANT DETAILS

C57BL/6 (strain 000664) and 5 \times FAD (strain 34840) mice were purchased from the Jackson Laboratories and maintained in our facilities. Mice bearing knock-in of human APOE2, APOE3, or APOE4 in the murine *Apoe* locus [B6.129P2-*Apoe*^{tm1(APOE*2)Mae} N9 (APOE2), B6.129P2-*Apoe*^{tm2(APOE*3)Mae} N8 (APOE3) and B6.129P2-*Apoe*^{tm3(APOE*4)Mae} N8 (APOE4)] were purchased from Taconic Biosciences and maintained in our facilities. Mice expressing each APOE allele were crossed with 5 \times FAD hemizygous mice to generate the final AD*APOE line. 5 \times FAD hemizygous*APOE homozygous mice were used in this study. Mice were weaned at the third postnatal week, genotyped in-house and kept on a 12 h/12 h light/dark cycle (lights on at 7:00) with access to food and water ad libitum.

Both female and male mice were used for experiments. Animal care and experimentation were according to NIH guidelines and were approved by the Institutional Animal Care and Use Committee at The Rockefeller University (protocols #20010 and #23007).

METHOD DETAILS**Brain immune cell isolation**

Brain immune cells were isolated as previously described^{97–100} with minor modifications. Briefly, mice were anesthetized with a ketamine/xylazine cocktail and perfused with 25 ml of Ca2+/Mg2+-free DPBS (Sigma). Cortex and hippocampus were removed and placed in FACS buffer (PBS containing 5% FBS and 10 mM HEPES), minced with scissors, and incubated with 80 U/mL of collagenase D (Roche) at 37°C for 30 min. Collagenase was inactivated by adding 10 mM EDTA for an additional 5min incubation at 37°C. Digested material was passed through a 70 μ m cell strainer and centrifuged at 1500rpm for 10min. The pellet was then resuspended in 7mL of 38% Percoll (Sigma) followed by a centrifugation at 2000rpm for 30 min. Nonspecific binding to Fc receptors was blocked by incubation with a CD16- and CD32-specific antibody (BioLegend) for 15min. Lastly, cells were washed and stained with an anti-CD45 antibody (BioLegend) and 0.05 μ g/mL DAPI (Sigma), then washed and resuspended in FACS buffer. Cells were sorted on a FACSAria-II flow cytometer (Becton, Dickinson) for singlet DAPI $^+$ Cd45 $^+$ cells.

Single-cell library preparation

For samples from 96-week-old mice, sorted CD45 $^+$ cells from each genotype were washed, strained through a 40 μ m strainer (Flowmi), and resuspended in PBS containing 0.04% BSA at ~1000 cells/ μ L. Libraries were prepared using 10X Genomics 3'v3 chemistry per manufacturer's instructions and sequenced on an Illumina NovaSeq SP. Six mice were pooled for the APOE3 library while four mice were pooled for the APOE4 library.

For samples from 10-week-old and 20-week-old mice, cells were also stained with 0.5 μ g of TotalSeq-C mouse hashing antibody (BioLegend) per genotype before cell sorting. Sorted CD45 $^+$ cells from each genotype were then pooled at equal cell numbers, washed, strained through a 40 μ m strainer (Flowmi), and resuspended in PBS containing 0.04% BSA at ~1500 cells/ μ L for superloading as previously described.¹⁰¹ Libraries were prepared using 10x Genomics 5'v2 chemistry with Feature Barcoding per manufacturer's instructions and sequenced on an Illumina NovaSeq SP. Three mice were pooled together per genotype for each library.

Aducanumab treatment and library preparation

For the aducanumab treatment experiment, 60-week-old mice were treated intraperitoneally with 0.5mg of either aducanumab (Cerebral Health) or human IgG isotype control (Invitrogen #02-7102) daily for 5 days prior to immune cell isolation and library prep as for the 10-week-old and 20-week-old mice, ultimately pooling cells at ~2000 cells/ μ L for superloading. Samples were sequenced on an Illumina NovaSeq S2. Three mice were pooled together per genotype for each library.

Multome library preparation

Brain immune cells were isolated as described above from two 60-week-old AD⁺APOE4 mice. Sorted CD45⁺ cells were centrifuged at 500rcf for 5min at 4°C and resuspended in 100µL lysis buffer (10mM Tris-HCl pH 7.4, 10mM NaCl, 3mM MgCl₂, 0.01% Tween-20, 0.01% Nonidet P40 substitute, 0.001% digitonin, 1% BSA, 1mM DTT, and 1U/µL Sigma Protector RNase inhibitor in nuclease-free water). Cells were lysed for 3min on ice. Lysis was stopped by addition of 1mL wash buffer (10mM Tris-HCl pH 7.4, 10mM NaCl, 3mM MgCl₂, 1% BSA, 0.1% Tween-20, 1mM DTT, and 1U/µL Sigma Protector RNase inhibitor in nuclease-free water) followed by centrifugation at 500rcf for 5min at 4°C. Cells were washed twice more in wash buffer, then resuspended at 3000 nuclei/µL in diluted nuclei buffer (10X Genomics nuclei buffer diluted with 1mM DTT and 1U/µL Sigma Protector RNase inhibitor in nuclease-free water). Libraries were prepared using 10X Genomics Single Cell Multome ATAC + Gene Expression chemistry per manufacturer instructions. The GEX library was sequenced on an Illumina Nextseq P2, while the ATAC library was sequenced on an Illumina NovaSeq S1.

Bulk sequencing of neuroimmune cells

Brain immune cells (Cd45⁺) were isolated from five 60-week-old mice per genotype as for single-cell library preparation but sorted directly into 500µL of Buffer RLT (Qiagen). Each brain was sorted into a separate tube rather than bulking genotypes together. RNA was isolated using the RNeasy Micro Kit (Qiagen) and used as input for library preparation using the SMART-Seq v4 Low Input workflow (Takara Bio). Samples were sequenced on an Illumina NovaSeq SP. The resulting FASTQs were processed with Salmon⁹⁶ to generate per-sample counts matrices, followed by *in silico* decomposition against the atlas using Bisque.³³

Paraffin embedded sections of human brains

Human brain sections of postmortem age-matched Alzheimer's disease APOE3/APOE3 carriers and APOE4/APOE4 carriers were obtained from the Carroll A. Campbell, Jr. Neuropathology Laboratory at the Medical University of South Carolina, which is part of the South Carolina Alzheimer's Disease Research Center. The experiments involving these sections were reviewed and approved by the IRB committee of the Medical University of South Carolina (eIRB Pro0012869). This study met the "Not Human Research" criteria defined by the Code of Federal Regulations (45CFR46).

APOE genotyping

APOE alleles were genotyped as previously described.¹⁰² In short, genomic DNA was extracted from 10–20g pieces of brain tissue using the E.Z. 96 Tissue DNA Kit (Omega Bio-Tek). The APOE locus was amplified using the forward primer 5'-ACAGAAT TCGCCCCGGCCTGGTACAC-3' and the reverse primer 5'-TAAGCTTGGCACGGCTGTCCAAGGA-3' with the following thermocycling settings: 94°C 3min, (94°C 30s → 60°C 30s → 72°C 1min) × 35 cycles, 72°C 2min, 12°C hold. Amplicons were digested by addition of 0.165µL each of AflII (New England Biolabs) and HaeII (New England Biolabs) and incubation for 120min at 37°C. The resulting digests were run on a 4% agarose gel to differentiate between the characteristic banding patterns.

Xenium library preparation

Sections were prepared from FFPE blocks of cortical tissue from human AD donors, acquired from the Carroll A. Campbell, Jr. Neuropathology Laboratory, which is part of the South Carolina Alzheimer's Disease Research Center. Sample preparation and imaging was performed as per manufacturer recommendations using the Human Brain Gene Expression Panel (10X Genomics).

Methoxy-X04 staining

After the Xenium workflow, slides were subjected to the manufacturer's quencher removal protocol used for post-Xenium H&E staining. After quencher removal, slides were stained for 10min in 30µM methoxy-X04 (Tocris Bioscience) solution in 40% EtOH, adjusted to pH 10 with NaOH. Slides were dipped briefly in water 5× before being differentiated for 2min in 0.2% NaOH in 80% EtOH. Sections were then stained with 1:10,000 STYOX Green (ThermoFischer) in HBSS for 10min to mark nuclei. Slides were washed 3× in water before being imaged in 405nm and 488nm channels.

Aβ uptake experiment

Single-cell suspensions were generated from the hippocampal and cortical regions of the brains of 60-week-old mice as previously described. Aβ 1-42, HiLexa™ Fluor 488-labeled (Anaspec #AS-65627) was used for Aβ oligomer preparation (denoted AβO-488). Aβ oligomers were prepared according to Ledo et al.¹⁰³ Cells were treated with 1µM of AβO-488 per 15 min at RT before being washed and sorted on a FACSaria-II and gated for singlet DAPI⁻ Cd45⁺ cells. Within this population, cells were sorted into either AβO-488-hi or AβO-488-lo pools depending on whether they were in the top or bottom 50% of AF488 signal. Sorted cells were spun down at 300rcf for 7min at 4°C, resuspended in 100µL FACS buffer containing 0.5µg of TotalSeq-C mouse hashing antibody, and incubated on ice for 15 min. Cells were then washed twice more in FACS buffer before counting, pooling at equal numbers, and resuspending at ~2000 cells/µL for single-cell library preparation with superloading using 10X Genomics 5'v2 chemistry per manufacturer instructions. Three mice were pooled together per genotype for each library.

Library analysis

Counts matrices were produced using Cell Ranger version 6.1.1 with alignment against mm10 as a reference genome. For multiplexed samples, hashed demultiplexing was performed using Cell Ranger multi, with read R2 and pattern 5PNNNNNNNNN(BC). Hashing sequences used for each sample are provided in [Table S1](#).

All code used for subsequent bioinformatic analysis is provided; briefly, data from single-cell libraries was loaded into Seurat,⁹³ filtered by QC metrics such as fraction of reads with mitochondrial origin, number of reads, and number of unique features using MiQC,²⁸ and integrated by Seurat rPCA integration to generate a single dataset encompassing cells from 10-week, 20-week, and 96-week samples (E2_10wk: 3,494 cells; E3_10wk: 3,523 cells; E4_10wk: 3,344 cells; E2_20wk: 2,997 cells; E3_20wk: 3,685 cells; E4_20wk: 4,634 cells; E3_96wk: 6,745 cells; E4_96wk: 2,446 cells). This structure was clustered and manually annotated to arrive at the final, analyzed data structure. Data from the aducanumab and A β libraries were analyzed and processed using the same method as was used for the atlas.

Data from the multiome library was loaded into Signac⁵⁰ and filtered manually by QC metrics such as fraction of reads with mitochondrial origin, number of GEX reads, number of ATAC reads, number of unique features, TSS enrichment, and nucleosome signal. Peaks were called using MACS2.⁹⁴ The resulting GEX and peak information were used to generate a joint UMAP representation via Seurat's weighted nearest neighbor approach. After clustering and manual annotation, peaks were re-called within each cluster to identify rare, cluster-specific peaks to arrive at the final, analyzed data structure.

For all downstream analysis, please refer to the accompanying code documentation.

Spatial transcriptome analysis

Preprocessing and cell segmentation of Xenium data was performed by the onboard pipelines on the Xenium machine. The resulting counts matrices were loaded into Squidpy,⁶⁸ log-normalized, and filtered to cells with at least 5 transcripts and to genes with expression in at least 5 cells. As all libraries were generated from the same source and on the same machine run, data were merged without computational integration. This data was clustered and manually annotated to arrive at a final data structure. Markers for each cluster were identified by filtering the microglial atlas to only the genes probed by the utilized Xenium panel and using conventional differential gene analysis methods such as the FindMarkers function to identify putative markers of each population.

Single-cell density plots

Density plots were generated by retrieving the raw UMAP cell embeddings from the Seurat structure. The ggplot::stat_density_2d function was then used to calculate the two-dimensional kernel density estimated with an axis-aligned bivariate normal kernel evaluated on a square grid.

RNA velocity analysis

Raw reads from the single-cell library were realigned against the mouse transcriptome in splice-aware fashion using the kallisto bus-tools kb-python workflow.³⁰ Spliced and unspliced matrices were then imported into Python alongside barcodes, UMAP coordinates, and cluster information previously calculated as described above. Matrices were filtered to remove empty droplets and merged with UMAP and cluster data before being processed with scVelo⁹⁵ in dynamical modeling mode. The top 100 genes were corrected for differential kinetics before the calculation of velocity for each individual cell.

The velocity calculated by scVelo was then used as an input for CellRank³¹ to construct a custom kernel. Alongside the velocity kernel, a connectivity kernel based on k-nearest neighbors, a pseudotime kernel, and a kernel built from CytoTRACE³² were included at a ratio of 2%, 90%, 4%, and 4%, respectively. GPCCA was used to estimate flow through the kernel via Schur decomposition with the Krylov method on 10 components, with five terminal macrostates identified. This kernel and estimation were used for downstream analysis.

Ligand-receptor analysis

For the microglial atlas and the multiome dataset, CellPhoneDB⁴⁰ was used to estimate ligand-receptor interactions. Raw counts were normalized to counts per 10,000 per cell and gene names were converted to human orthologs using the MGI human-mouse ortholog dataset. CellPhoneDB was run in statistical_analysis mode against the CellPhoneDBv3 database using default parameters. Statistical significance was evaluated by CellPhoneDB's internal bootstrapping method and only significant interactions were used for downstream analysis.

For the aducanumab treatment dataset, CellChat⁷¹ was used to estimate ligand-receptor interactions. For each sample in the integrated dataset, a CellChat object was generated, overexpressed genes and interactions were identified, and communication probabilities and pathways were computed. These CellChat objects were then lifted onto the same cluster labels using the liftCellChat method before being merged for later analysis. All interactions were estimated from raw counts against the CellChatDB.mouse object with default parameters.

Transcription factor program analysis

SCENIC³⁴ and SCENIC+⁵³ were used to perform transcription factor regulatory program estimation on single-cell and multiome data, respectively. For SCENIC, GRNBoost2 was used to identify coexpressed modules from the raw counts data. RCisTarget was then used to identify regulons before AUCell was used to estimate the activity of each regulon at single-cell resolution. The output matrix of

regulons by cells was used for downstream plotting and analysis. Differential module analysis was performed by importing the regulon-by-cell matrix as a Seurat assay and performing conventional differential expression analysis via Wilcoxon rank sum test.

For SCENIC+, raw counts were imported along with cluster annotations. RNA counts were log-normalized, scaled, and filtered to highly variable genes. Raw ATAC reads were imported and peaks were called normalized to the size of each chromosome using MACS2 before being filtered using the Aerts Lab mm10 blacklist. Consensus peaks were converted to a bed file for downstream analysis. Processed RNA and ATAC data were subjected to QC controlling for fragment count, FRIP, TSS enrichment, and duplication rate to filter to high-quality cells. CisTopic was used to perform latent Dirichlet allocation topic modeling before PyCisTarget was used to identify enriched motifs and differentially accessible regions. These results were used as inputs to the SCENIC+ algorithm against a list of all known mouse transcription factors from the HUST database. Estimated gene regulatory networks were used for downstream analysis. For *in silico* perturbation modeling, the plot_perturbation_effect_in_embedding function was used to re-estimate transcriptional profiles after setting the expression of a given transcription factor to 0.

Multome topic modeling

The MIRA suite⁵² was used to perform topic modeling and latent Dirichlet allocation on multome RNA and ATAC data. Raw RNA and ATAC counts were filtered to genes with expression at least 15 cells and normalized to 1000 total counts per cell. Genes were separated into highly variable genes based on dispersion for training of each topic model. These models were then used to generate a joint representation of RNA and ATAC features with a box-cox transformation strength of 0.33 selected by examining the quality of the resulting UMAPs, per MIRA documentation recommendations. Clusters were renamed to match clusters from the Seurat-generated joint representation before per-cell topic scores for all RNA and ATAC topics were exported and used for downstream analysis.

Bulk sequencing decomposition

Bisque³³ was used to decompose bulk RNA sequencing counts into estimates of population frequencies. After reads were aligned with Salmon, counts were merged into a single table for later analysis. Raw counts from the integrated single-cell atlas were used as a reference for Bisque decomposition via the SeuratToExpressionSet function. The bulk table was then decomposed with no prespecified markers. The resulting proportion estimates were used for later plotting and analysis.

Metabolic state estimation

Compass⁴⁹ was used to estimate the flux through each metabolic reaction in Recon2 in the atlas and multome datasets. In order to decrease computational demands and to reduce the impact of signal sparsity, fifty cells for the atlas or ten cells for the multome dataset from each cluster were randomly pseudobulked together. Raw counts were then exported and used as input to Compass on all *Mus musculus* reactions with default parameters. The IBM ILOG CPLEX Optimization Studio was used with an academic license to solve flux balance analysis.

QUANTIFICATION AND STATISTICAL ANALYSIS

R version ≥ 4.1 and Python version ≥ 3.7 were used for data analysis. FlowJo software (Tree Star) was used for analysis of flow cytometry data. No statistical methods were used to predetermine sample sizes; sample sizes were determined according to data reported in previous publications. Animals in the same litter were randomly assigned to different experimental groups and blinded to experimenters.